Manufacture and Characterization of Additively Manufactured Ceramic Electromagnetic Structures

Richard L. Dumene

Thesis submitted to the faculty of the Virginia Polytechnic Institute and State University in partial fulfillment of the requirement for the degree

of

Masters of Science

in

Electrical Engineering

Gregory D. Earle, Chair

Christopher B. Williams, Co-Chair

Joseph B. Baker

April 30, 2018

Blacksburg, VA

Keywords: Metamaterials, Ceramics, Dielectrics, 3D Printing, Ferrite

Manufacture and Characterization of Additively Manufactured Ceramic Electromagnetic Structures

Richard Dumene

ABSTRACT

Additive Manufacturing (AM, also known as 3D printing) can produce novel three-dimensional structures using low-loss dielectric materials. This enables the construction of dielectrics with complex shapes that enable innovative microwave applications such as resonators, filters, and metamaterial lenses. This thesis addresses the production and characterization of cellular structures of various designed densities created with a low loss ceramic material, alumina (aluminum oxide), via vat photopolymerization. The permittivity of these printed structures is variable over roughly an octave, with a range of relative permittivites from 1.78 to 3.60, controlled via part geometry. Two additional materials, ferrite and nickel, have been explored for inclusion within these dielectric structures to enable the production of multi-material electromagnetic structures with conductive, magnetic, and dielectric elements.

Manufacture and Characterization of Additively Manufactured Ceramic Electromagnetic Structures

Richard Dumene

GENERAL AUDIENCE ABSTRACT

Additive Manufacturing (AM, also known as 3D printing) has unique manufacturing capabilities. 3D printing can create structures that cannot be produced using traditional manufacturing methods. For example, sponge like structures, with internal voids inaccessible from the outside of the structure, can be created out of a variety of materials. Such structures, known as cellular structures, can be used to create new advanced materials.

Ceramic cellular structures can be produced using 3D printing. Ceramics possess many advantages over other materials for use in high frequency radio systems, such as those used for radar and communications. Notably, ceramics are known as low-loss materials, meaning that when electromagnetic waves travel through them they lose less energy than other materials.

Cellular structures can be used to vary a material property known as the dielectric constant. Creating cellular structures with designed dielectric constants will enable the creation of new and useful electromagnetic structures. Measuring how this material property changes with the geometry of the cellular structures is important to enable their use. These measurements are described in this work.

Additionally, other materials are printed into the ceramic structures. Ferrite, a magnetic material, is extruded as a paste from a nozzle into the ceramic structures. This material is also important for radio systems. Nickel, a good conductor, has also been embedded into the ceramic to provide the ability to create electrically conductive paths inside the part.

ACKNOWLEDGEMENTS

The author would like to acknowledge the help and support of colleagues in the DREAMS Lab at Virginia Tech, including Dr. Donald Aduba Jr. and Logan Sturm, as well as Paul Kennedy and Ali Hosseini Fahraji for their assistance over the course of this work. I would also like to acknowledge Dr. Majid Manteghi for providing waveguide segments and the network analyzer used to perform measurements of the dielectric constant, and Nottingham University for providing the FlatPack software used to generate the cellular structures. The author would like to acknowledge Dr. Guo-Quan Lu for generously providing a photo reactive ferrite paste. Additionally, I acknowledge the support provided to this work by the Virginia Space Grant Consortium.

TABLE OF CONTENTS

LIST OF FIGURES

LIST OF TABLES

LIST OF EQUATIONS

1 – INTRODUCTION

1.1 MOTIVATION AND RESEARCH GOALS

With ever-increasing demand for faster and more robust communication systems, high performance, low loss electromagnetic (EM) structures show great promise in the improvement of such systems. Production of high performance EM structures is often expensive and slow, with many procedures being performed by highly skilled technicians to ensure reliable device performance. With the maturation of Additive Manufacturing (AM) technologies, it is possible to more easily create high performance EM structures with complex geometries and potentially reduced production costs.

Additive manufacturing has shown great promise in the production of metamaterial structures (further defined in section 1.4.2) and high performance materials, such as ceramics. Currently, the production of metamaterials is expensive and limited to specific types of structures. AM has the potential to greatly expand the variety of metamaterial structures produced and dramatically lower the costs to do so. Metamaterial structures created from high performance, robust materials, have the potential to withstand harsh environments, including corrosive and very high heat environments, potentially enabling the use of these high performance structures to place radar and communication systems locations that would damage or destroy other high frequency systems.

1.2 RESEARCH OBJECTIVES AND CONTRIBUTION

This research seeks to explore the application of advanced additive manufacturing technologies to create high quality low loss ceramic dielectric materials suitable for use in metamaterial

applications. The main objective of this research is to characterize the ability of AM to create compound dielectric structures with properties defined by easily manipulated design parameters. Cellular structures with designed internal voids are used to create dielectrics consisting of an alumina lattice and periodically spaced air voids. The effective dielectric constant of these structures is evaluated in the X-band, and their loss tangents are measured using waveguide sections filled by the structures. The effective dielectric constant of the structure is determined by the fraction of the volume of the structure that is constructed of alumina.

By keeping the cellular feature sizes small relative to the wavelength of interest, the effective dielectric constants can be predicted by the Wiener bounds (section 1.5.3). This work seeks to confirm these predictions, determine if a feature size of $1/10^{th}$ of the wavelength of interest is sufficiently small, and determine where within the Wiener bounds the measured values lie. This characterization will enable the production of tailored dielectrics with arbitrary effective dielectric constants between an upper value defined by the bulk effective dielectric constant of the alumina and the dielectric constant of air. By extension, this process will enable the free-form placement of arbitrary dielectric regions within a volume, which may have applications in the creation of high frequency lenses, cavity resonators, and filters.

1.3 Overview of Additive Manufacturing

Additive Manufacturing (AM), also known as 3D printing, is well known for its ability to produce structures that are impossible to create via traditional manufacturing processes such as subtractive machining and casting. A diverse set of materials can be produced via AM, including polymers, ceramics, and metals, and it is often possible to create composite structures of these

materials. AM is a flexible and powerful tool that provides freedom to design unique and novel structures.

The AM process begins with a 3D computer model of the desired part. Specialized slicing software converts this model from a three-dimensional shape into a series of two-dimensional cross-sectional layers based on the desired machine and process parameters. These layers are then processed into a machine code that controls the printer, similar to other computer aided manufacturing (CAM) systems. The printer then creates parts layer-by-layer, by selectively depositing or fusing material. Figure 1 illustrates this process.

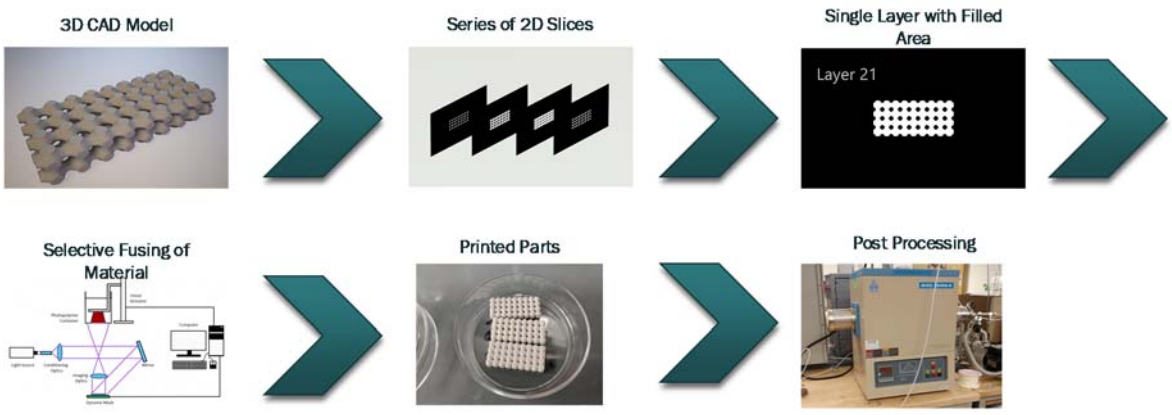

Figure 1: Additive Manufacturing (3D Printing)

This process is diametrically opposed to traditional subtractive manufacturing techniques. Even the most advanced computer numerically controlled (CNC) mill must start with a solid block of material, and is limited in what potential tool paths it can follow. AM enables the production of unique structures, including those with enclosed cavities and/or periodic or irregularly spaced small-scale cells or lattices, such as the cellular structure shown in Figure 2, not normally producible via subtractive manufacturing.

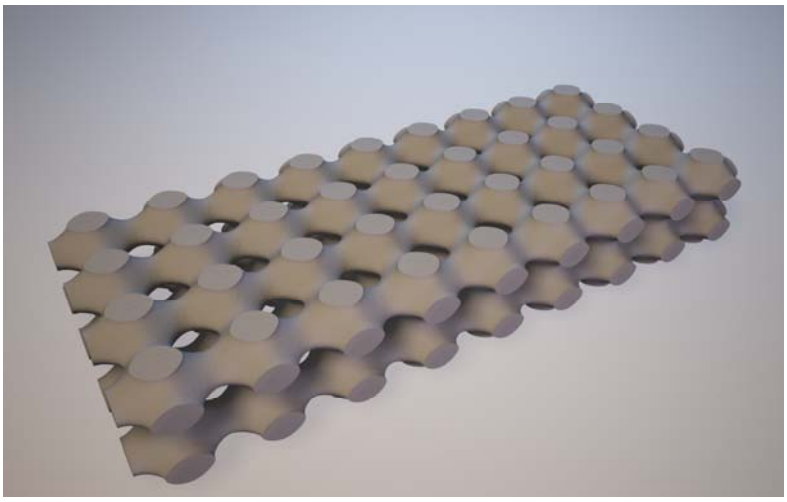

Figure 2: Cellular Structure

AM is currently used in many industries to create high-performance parts, enable rapid prototyping, and to build end use parts in low to medium volume. It is proving to be a powerful technology that enables continued improvements to the state of the art in manufacturing and fields that are limited by manufacturing technologies.

1.3.1 Overview of AM Processes

Multiple AM processes exist, and all have unique strengths and weaknesses. Thermoplastic extrusion (FDM), which is pictured in Figure 3 (Left), is a printing process where molten thermoplastic is extruded through a moving build head to create a series of extruded thermoplastic lines, known as roads, to fill the layer. While FDM is common, other processes enable the production of structures with smaller feature sizes, smoother surfaces, and more robust materials. The powder-bed fusion (PBF) and binder jetting (BJ) processes create parts using a bed of powder [1]. In these processes, the powder is first spread across the top of the previous layer and then selectively adhered to the previous layers through the application of a chemical binder or heat. An example of a binder jetting system is shown in Figure 3 (Right).

Powder is rolled across each layer from a powder reservoir and bound together with a polymer binding agent using an inkjet head (BJ), or through selective application of heat (PBF).

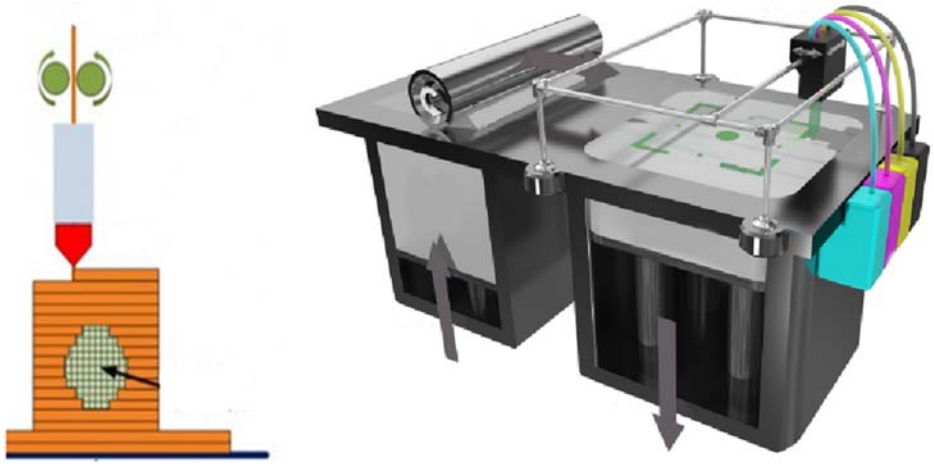

Figure 3: Extrusion (Left) and Powder Bed Printing (Right)

Material jetting and Vat Photopolymerization (VP) (also known as stereo-lithography-apparatuses (SLA)) can be used to create structures from UV curable photopolymers cured from a vat of resin. The material jetting process involves the precise deposition of material from a print head, similar to common inkjet printing, with an additional Z-dimension [2]. VP processes make use of a vat of UV reactive resin. The resin in this vat is selectively exposed to UV light, causing selective curing of the resin on each layer. During the printing process, the build platform is gradually moved to successively expose the top layer of the part to fresh resin and the UV light source required to cure it. The build platform may either ascend from the resin vat, or descend into the vat. A descending build platform uses UV light shown from above to cure the parts; these systems are known as top-down systems (Figure 4, Left). In contrast, an ascending build platform uses UV light shown from below through a window in the bottom of the vat (Figure 4, Right). These cured resins polymerize to each other creating a polymer structure.

Photopolymer-ceramic suspensions can be created and cured, where the photopolymer acts as a temporary support structure for the material suspended within it [1]. Creating suspensions in such a manner and preforming appropriate post-processing enables the creation of ceramic and metallic structures with these technologies [3]. If materials with compatible properties are used, composite structures can be created using a combination of these processes. A further exploration of these processes is presented in chapter 3.

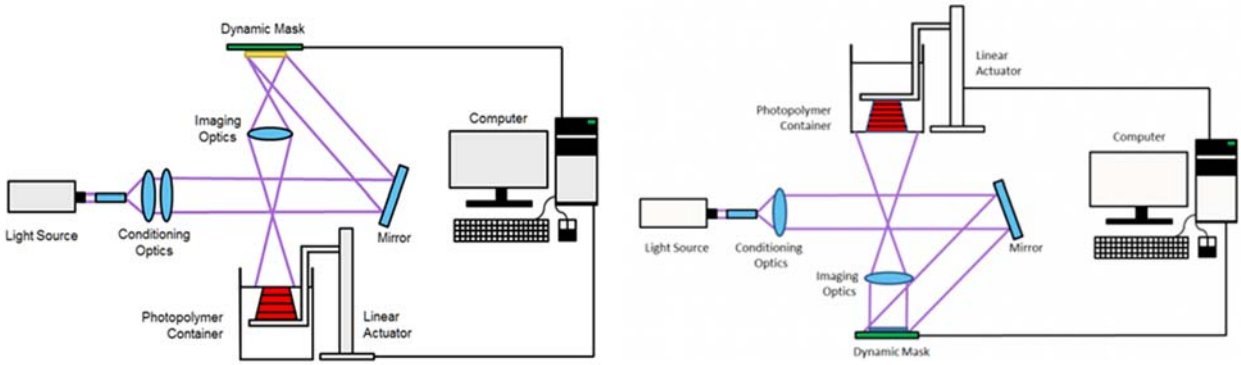

Figure 4: Top Down (Left) and Bottom Up (Right) Vat Photopolymerization

This work explores the use of VP and paste extrusion systems for the creation of composite structures for high frequency electronic applications. These processes were chosen because of their ability to operate at room temperature, their ability to produce ceramic and metallic structures, and their ability to create precision parts with small feature sizes and good surface finishes [3].

1.3.2 Density

There are three different measurements of density of interest to this work, which we denote as the effective density, the relative density, and the bulk density.

$$\rho_{Eff} = \rho_{bulk} * \rho_{relative} \quad (1)$$

The effective density of a printed part (ρ_{Eff}) is the total mass of the part divided by the volume of the bounding box of the space the printed part occupies. This density represents the overall part mass to volume ratio, including both designed internal voids, and microstructure voids, as represented in Figure 5 by black and red regions, respectively. These two distinct types of voids are independently described by the bulk and relative densities of the structure, respectively.

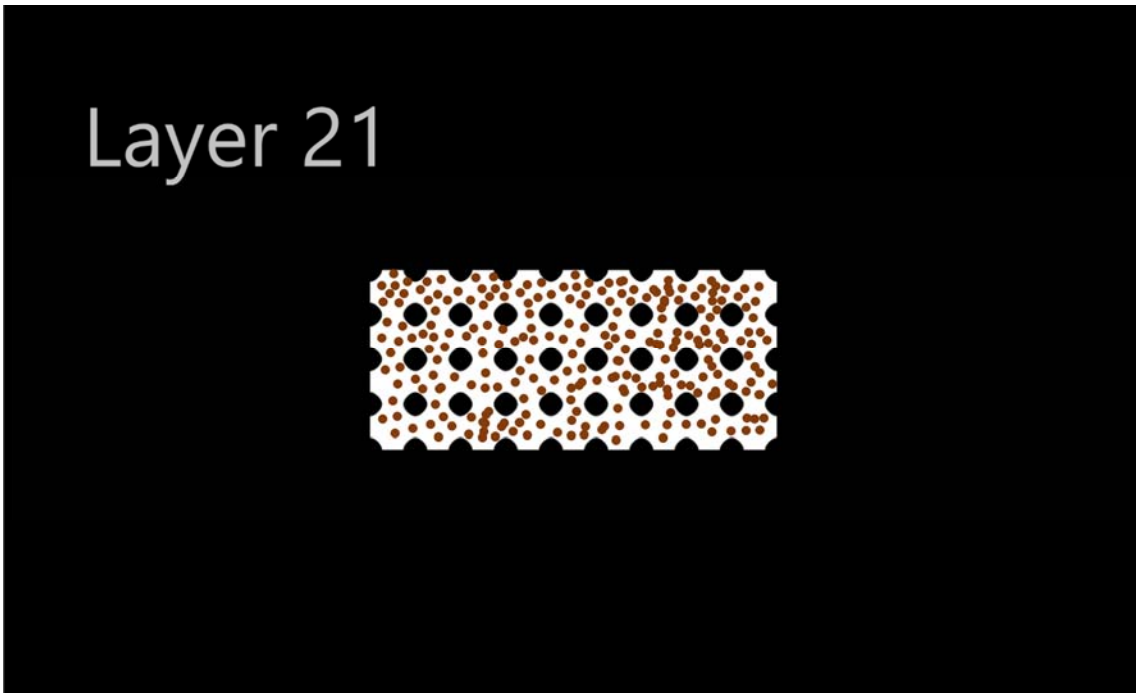

Figure 5: Graphical Representation of Part Structure, Large Designed Voids are shown in Black, Unintentional Microscopic Random Voids are shown in Red

The bulk density of a material (ρ_{bulk}) describes the density of a solid block of that material, including any microstructure voids and porosity (the red voids in Figure 5). It is best understood as the mass of a maximally solid printed sample divided by the volume of the sample. The bulk density can be most accurately determined using an Archimedes measurement, comparing the sample's mass to the volume of liquid the part displaces. In contrast, the relative density of the part ($\rho_{relative}$) describes the fraction of the overall volume of the bounding box that

is filled with printed material. This definition of density ignores any porosity in the microstructure and treats all of the printed volume of the part as completely solid. This measurement of density takes into account the designed (black) voids and ignores all unintentional (red) voids in Figure 5. The relative density is best understood as the fraction of the bounding box that is filled with printed material in the CAD model of the part.

The effective density is the density that ultimately affects the material properties. In this work, for example, electromagnetic waves interacting with the samples do not distinguish between intentional and unintentional voids. However, for a given printing process, the bulk density remains roughly constant, and the relative density can be easily varied by changing the CAD geometry. Thus, the effective density can be easily controlled through variation of the relative density.

1.4 HIGH FREQUENCY STRUCTURES AND METAMATERIALS

1.4.1 Overview of High Frequency Structures and Electromagnetic Theory

Novel structures often present great utility for use in high performance and high frequency electrical systems. Microwave and millimeter wave circuits are often constructed out of three-dimensional arrangements of dielectric, magnetic, and conductive materials. The unique design freedom AM provides enables the creation of structures that were previously difficult, or even impossible, to produce.

When creating a high frequency structure, the material properties of the conductive, dielectric, and magnetic elements are of great importance. The performance of dielectric and

nonmagnetic conductor materials is characterized by their complex permittivity *(2)*, as shown pictorially in Figure 6.

$$\epsilon = \epsilon' + j\epsilon'' \tag{2}$$

This parameter essentially describes the behavior of electric fields and currents within the material, where the real part of permittivity (*ε'*) is also known as the dielectric constant, which describes the ability of the material to store energy in an internal electric field. The imaginary part of the complex permittivity (*ε''*) is related to the conductivity of the material [4]. A perfect electric conductor has a purely imaginary permittivity with an infinite magnitude, while a lossless dielectric material has a purely real permittivity. The loss of a material can be easily defined as a loss tangent *(3)*, the ratio of the complex to real component of the permittivity, corresponding to the tangent of the angle δ. This loss tangent is also the inverse of the quality factor Q, which is best described as the ratio of the energy stored per cycle to the energy lost per cycle when the structure is excited by a high frequency field. [4]

$$tan(\delta) = \frac{\epsilon''}{\epsilon'} = \frac{1}{Q} \tag{3}$$

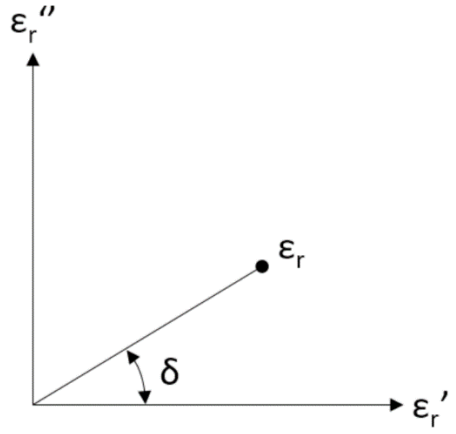

Figure 6: Complex Permittivity

Magnetic materials are also characterized by a quantity that is analogous to the permittivity. This parameter is μ, the magnetic permeability. Permeability is the dual parameter to permittivity that describes the ability of the material to support the formation of magnetic fields within the material. Nonmagnetic materials have a relative permeability of 1, corresponding the permeability of free space.

1.4.2 Metamaterials

Metamaterials possess uniquely engineered properties that are not found in natural materials. Such materials are often created with small-scale periodic composite structures. Metamaterials may exhibit unusual properties under their designed operating conditions. Examples include materials with graded or non-isotropic properties or negative refractive indexes. A negative index metamaterial structure is shown in Figure 7. This structure achieves the negative refractive index using arrays of split ring oscillators.

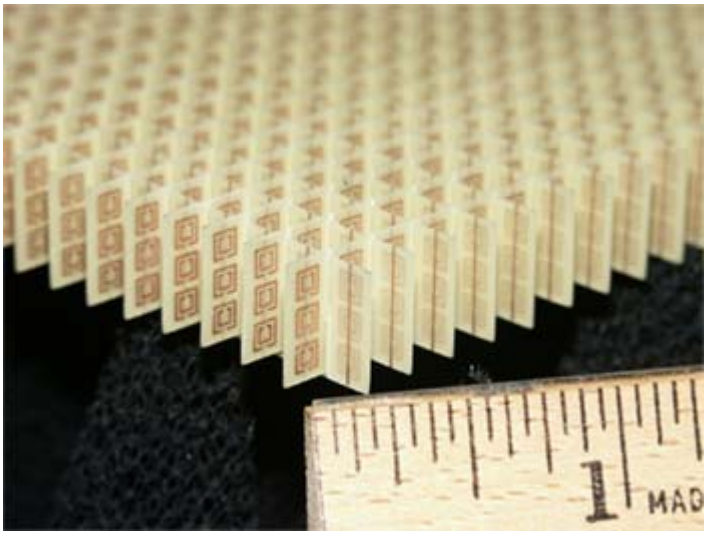

Figure 7: Split Ring Oscillator Based Metamaterial Structure [5]

Metamaterials possess unique utility for use in high frequency circuits. Such materials have many applications, and are often used as lenses or filters [6]. The performance of

metamaterial structures is determined by both the properties of the materials used to create them and the geometry of the structure. As such, AM is uniquely suited to the production of metamaterials due to the design freedom it provides in both material choice and physical structure, and the ability of AM to create structures with repetitive small scale features.

1.4.3 Wiener Bounds

Metamaterials are often created using non-homogenous media. The permittivity of such structures can vary wildly between different regions of the structure. While large-scale periodic variations in permittivity create complex wave propagation conditions, a material with variations in permittivity on scales small relative to the wavelength of interest can be treated as a homogenous medium. The effective dielectric constant of these pseudo-homogenous materials is bounded by upper and lower limits known as the Wiener bounds [7] [8]. The upper and lower bound equations are shown in equations *(4)* and *(5)*, respectively. Additionally, a plot of the upper and lower bounds for an arbitrary mixture of two materials is shown in Figure 8. This mixture consists of two materials with relative permitivitties denoted by the subscripts 1 and 2, where the volume fraction (ρ) represents the percentage of the mixture of the second material.

$$\epsilon_{UpperBound}(\rho) = \rho\epsilon_2 + (1-\rho)\epsilon_1 \tag{4}$$

$$\epsilon_{LowerBound}(\rho) = \left(\frac{\rho}{\epsilon_2} + \frac{1-\rho}{\epsilon_1}\right)^{-1} \tag{5}$$

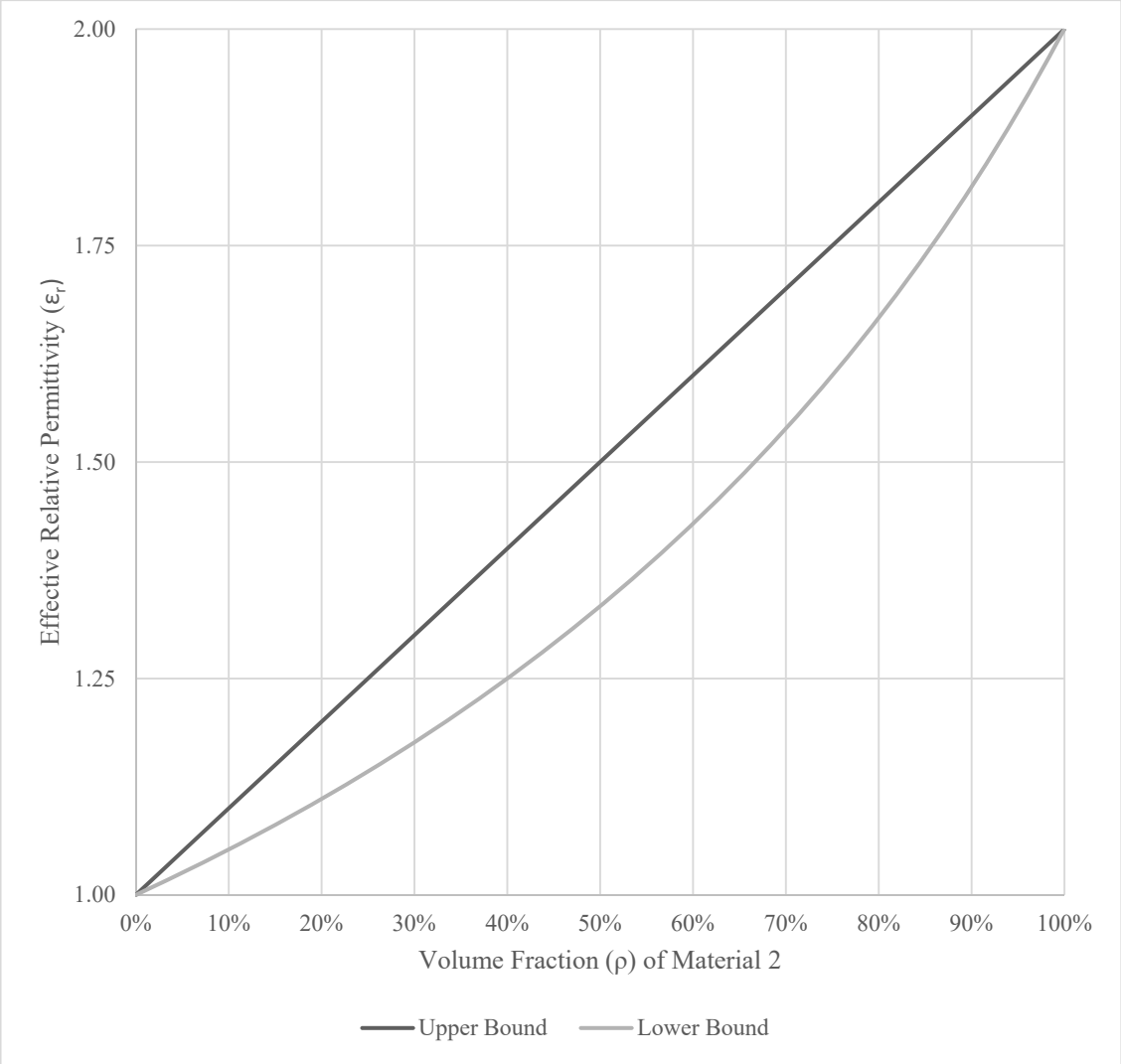

Figure 8: Plot of Upper and Lower Wiener Bounds of Mixture Consisting of Materials with Permittivites of 1 and 2

These upper and lower bounds are an application of the rule of mixtures [9] to the effective dielectric constant of the material. The upper and lower bound are most clearly analogous to the series and parallel addition of resistances. The upper bound is used when the direction of interest passes through discontinuities in the non-homogenous medium in series, such as normal to many stacked sheets, while the lower bound is used when the direction of interest passes along the discontinuities. These two extreme cases are shown in Figure 9. The lower bound applies to the example shown to the left, while the upper bound applies to the example shown to the right.

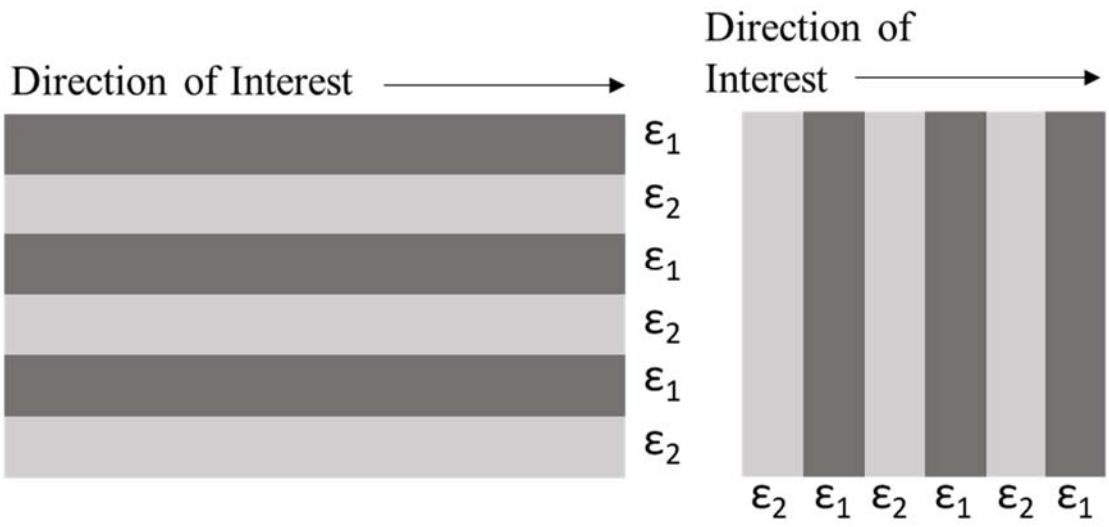

Figure 9: Extreme Cases, Lower Bound Case Pictured Left, Upper Bound Case Pictured Right

1.5 THESIS ORGANIZATION

The work presented in this thesis is organized as follows: This chapter has presented a general overview of AM processes, the specific processes used in this work, metamaterial structures, and the required background knowledge on the electromagnetic theory required to understand the goals and results. Its goal is to facilitate the understanding of the work presented later to someone unfamiliar with the specifics of AM or EM theory. Chapter 2 reviews the relevant literature on topics relevant to this work. Chapter 3 presents the design and manufacturing of the ceramic structures via AM. Chapter 4 reviews the measurement technique used to investigate the samples created using these processes, and describes the limitations of the measurement techniques. Additionally, data from these measurements are presented in this chapter. Chapter 6 discusses the use of new multi-modal printing techniques to extend the potential applications of this work to complex multi-material structures. Conclusions that can be drawn from this work are presented in chapter 7. Recommendations for future work are presented in chapter 8.

2 LITERATURE REVIEW

2.1 REVIEW OF RELEVANT LITERATURE ON MATERIAL PROPERTIES

2.1.1 Material Properties of Alumina

Alumina (Al_2O_3) is a commonly used ceramic in many applications. It has a high melting point (2040°C) and compressive strength (150-500 / >4000 MPa) [10, 11]. In addition to its exceptional mechanical properties, it is also a high performance dielectric, with an effective permittivity of ~9.1 and a very low loss tangent on the order of 10^{-4} [12, 13]. Ruby and sapphire are gemstone varieties of this material. Single crystal sapphire has been shown to be an exceptionally low loss dielectric when the crystal structure is correctly aligned with the applied electric field [13].

2.1.2 Effects of Microstructure of Alumina on Dielectric Properties

Studies have been performed on the effect of the microscopic porosity of alumina on both the relative permittivity and the loss tangent of the material. It has been shown that increases in the micro-porosity not only lower the permittivity of the material but also greatly increase the loss of the material [13]. The relationship between porosity and permittivity is linear and lies within the Weiner bounds. This relationship is shown in Figure 10. The trend line falls well below what the simple upper Wiener bound predicts.

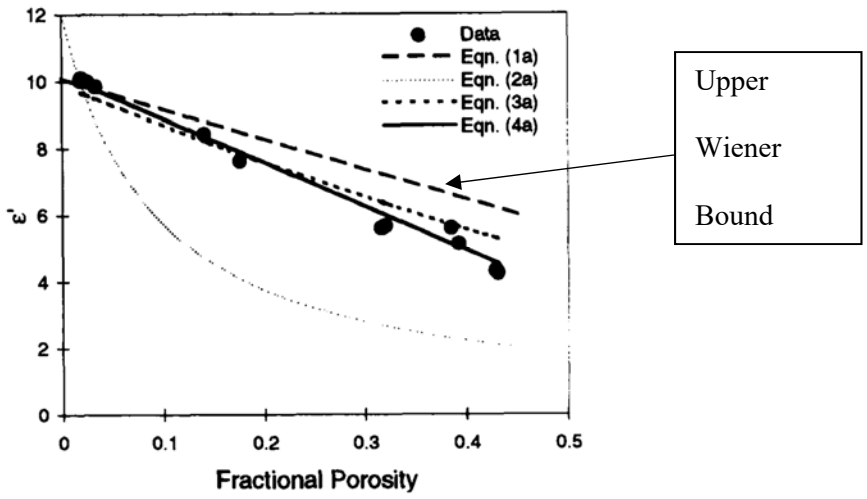

Figure 10: Permittivity of Alumina vs Microstructure Density [13]

2.2 ADDITIVELY MANUFACTURED ELECTROMAGNETIC STRUCTURES

2.2.1 Polymer and Polymer-Composite Structures

AM of polymer materials have been used to create a variety of EM structures. The author previously used additively manufactured photopolymer materials to construct various transmission lines and antennas [14]. These same materials have been used to create metamaterial Luneburg lenses [15]. A Luneburg lens relies on an intentional grading of the permittivity of the material from which it is constructed to create desirable refraction within the lens. A Luneburg lens has the interesting property of focusing a plane wave from any direction to a single point on the opposite side of the lens. An illustration of such a lens is shown below in Figure 11. The shading represents the effective permittivity of the lens and the lines represent the path of the wave through the lens.

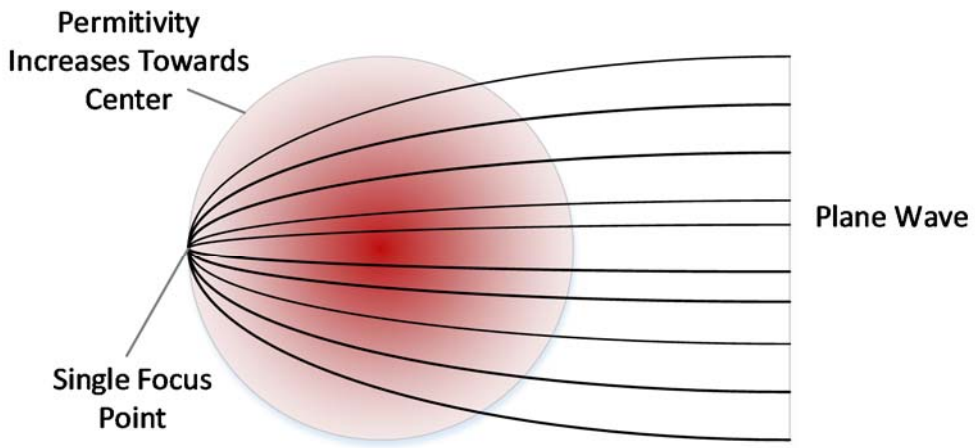

Figure 11: Luneburg Lens Focusing Plane Wave to Single Point

While such lenses have many applications for use as high performance antennas, their performance is dominated by the loss of the material from which they are constructed. The loss tangent of the material used to create these lenses has been shown to be very high, on the order of 10^{-2} [14]. This is comparable to the loss tangent of balsa wood.

Due to the moderately low values of relative permittivity for many polymers [14], efforts have been made to increase their effective permittivity by loading the polymer with high permittivity ceramics [7] [16]. The permittivity of the resulting composite varies linearly with the addition of the ceramic particles, allowing for a tunable permittivity of the material. Metamaterial structures have also been produced using this method, and behave within the range predicted by the Weiner bounds [8].

While these composite materials achieve high values of relative permittivity, they have been shown to be high loss, with loss tangents comparable to pure polymer structures [7] [16]. These high loss tangents limit the usability of the material, as gains generated by the use of these materials to create novel structures can be offset by the material loss itself.

2.2.2 Ceramic Structures

Pure ceramic EM structures have also been produced via AM. Vat photopolymerization of alumina suspensions has been shown to create high performance ceramic dielectrics with low loss tangents and high relative permittivity [17]. The general process for producing ceramic parts via VP AM is outlined in Figure 12. This thesis investigates the variation of the permittivity of similar structures as a function of the relative density of the structures.

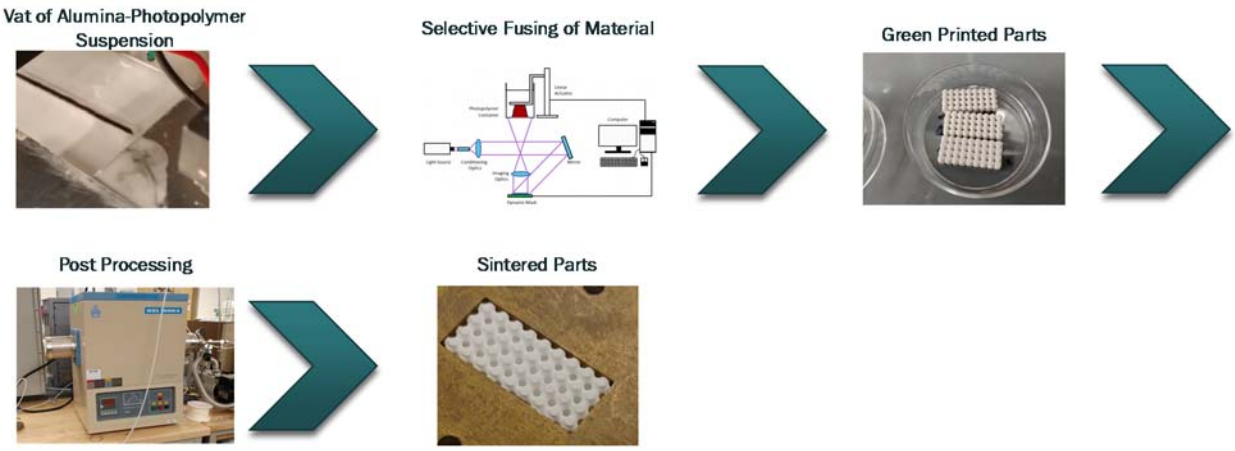

Figure 12: Ceramic Vat Photopolymerization Printing Process

3 DESIGN AND MANUFACTURING

3.1 DESIGN OF CELLULAR STRUCTURES

In order to enable effective characterization of the relative permittivity across relative density a variety of lattice structures at varying relative densities must be created. Structures are designed and created to meet a series of requirements that enable accurate measurement of their permittivity.

3.1.1 Requirements

The available waveguide segments and calibration kit (WR-90 waveguide) dictates that the frequency (and therefore wavelength) of testing should occur in the X-Band (8.0 – 12.0 GHz). The corresponding wavelengths of these frequencies are 3.75 cm and 2.50 cm (roughly 1.5” to 1.0”). As WR-90 waveguide has internal dimensions of 0.400” x 0.900”, and the waveguide flange selected for use as a sample holder has a length of 0.140”, a unit cell size of 0.100” x 0.100” x 0.070” was selected to enable a 4 x 9 x 2 lattice to fully fill the sample holder. The electrically short length of the sample, less than ¼ λ, was specifically chosen to eliminate measurement error related to ¼ λ effects and phase issues.

In addition to maximum size requirements, various other process limitations were accounted for. Primarily, to create voids within the part free of uncured slurry, an ‘open’ unit cell was chosen. This structure allows the uncured resin to either flow, or be rinsed out of the cavities in the part. It also helps to mitigate distortions in the sample geometries during the sintering process. Figure 13 provides an illustration of this requirement.

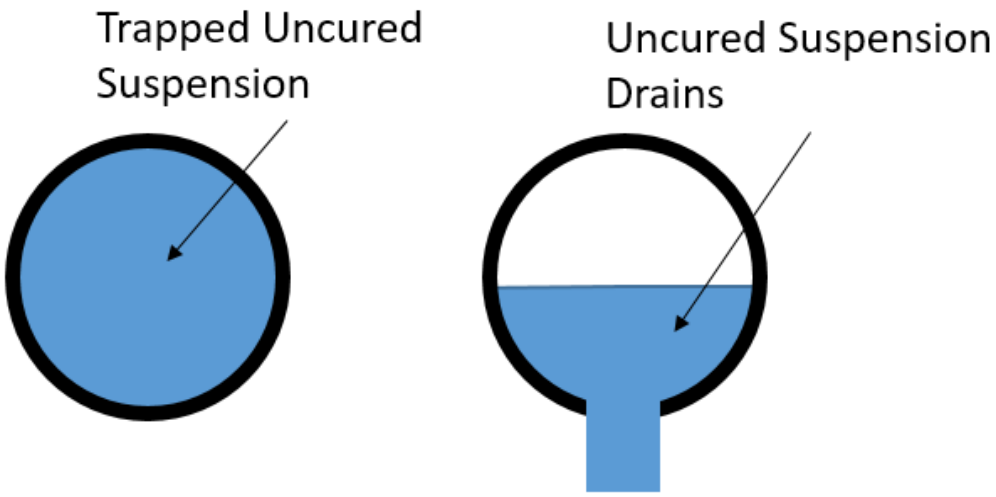

Figure 13: Closed Cell (Left), Open Cell (Right)

3.1.2 Flat Pack Software

Several structures with varying relative densities and similar maximal geometries are required for proper characterization, so a software solution for parametrically generating lattices was sought. Flat Pack, generously provided by the University of Nottingham, was selected to generate the lattices used for the desired structures.

Of the available unit cell geometries in Flat Pack (Figure 14), the network Schwartz cell was selected as it provided both an open structure and a relatively simple geometry, which reduces file complexity.

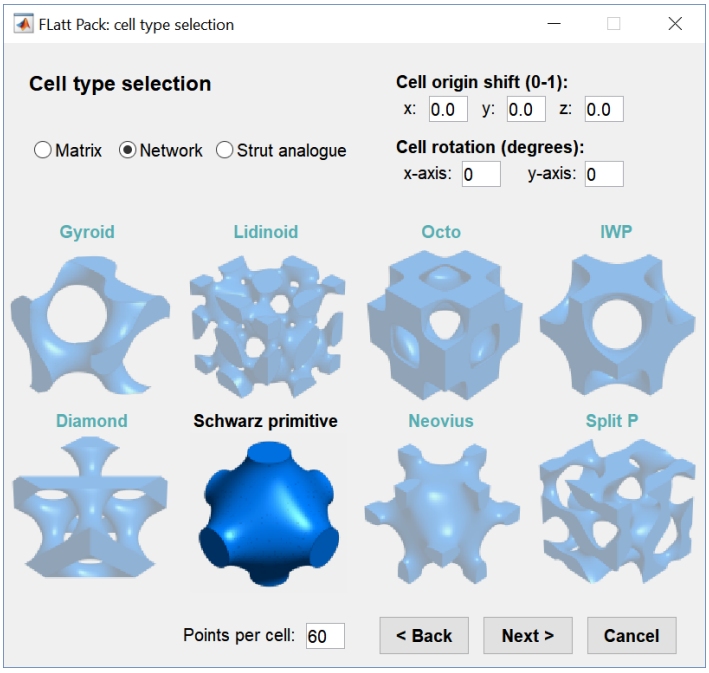

Figure 14: Flat Pack Unit Cells

Flat Pack was used to generate cellular structures with an external dimension of 0.400” x 0.900” x 0.140” and relative densities of 30%, 40%, 50%, 60%, and 70%. An example of a generated structure is shown in Figure 15.

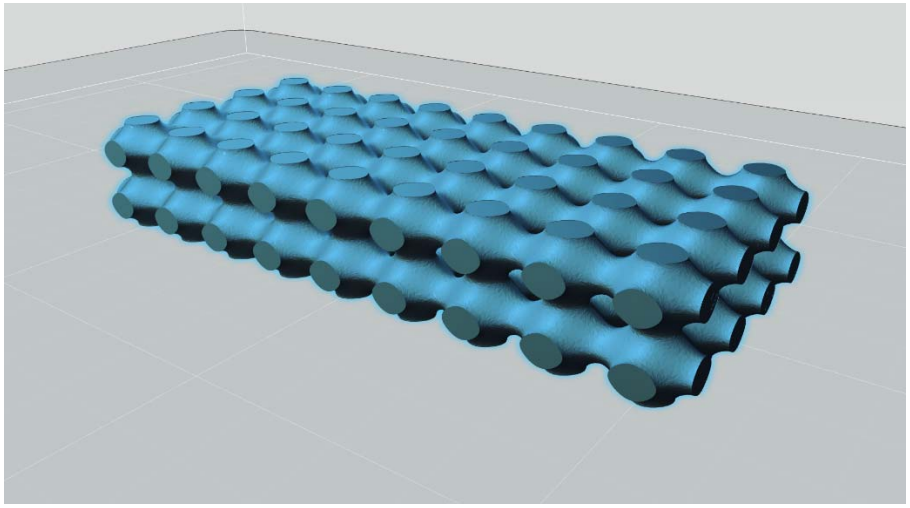

Figure 15: Example Flat Pack Generated Structure

3.1.3 Limitations

Structures with lattice densities of 10%, 20%, 80%, and 90% required the use of alternative unit cell geometries in order for the unit cells to remain both connected and open (Figure 16). These alternative unit cell geometries proved to be very complex, and created numerous errors in the Autodesk build preparation software (Print Studio). These errors precluded the production and testing of cellular structures at these lattice densities. In future work, simpler unit cell geometries or alternative build preparation workflows can be used to enable production of structures with these lattice densities.

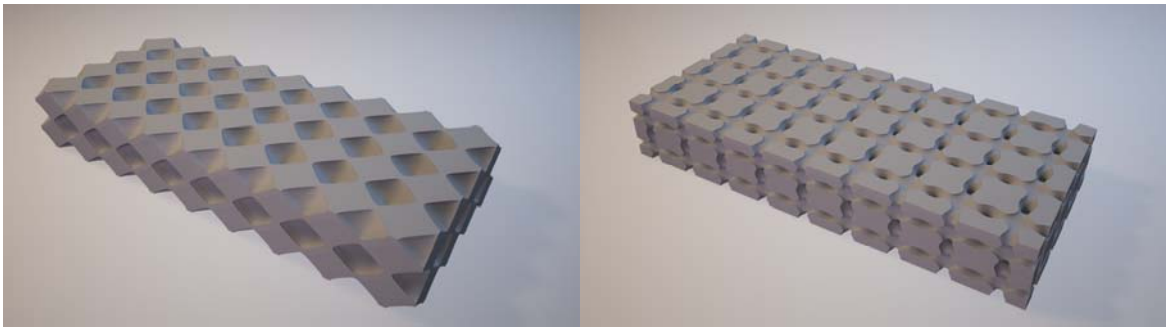

Figure 16: Example of Unintentionally 'Closed' Structure (Left), and Modified 'Open' Structure (Right)

3.2 VAT PHOTOPOLYMERIZATION OF ALUMINA

3.2.1 VP process for alumina

The VP process involves the selective curing of a photo reactive resin with a high intensity UV light source. In order to enable the production of ceramic structures using this method, a slurry is created consisting of a UV reactive resin and small alumina particles. The precise formula of this suspension is presented in section 3.2.2. This slurry, or suspension, is then processed identically to a traditional photopolymer resin, with the appropriate process parameters chosen to enable high quality parts. The result is commonly referred to as a green part. Green parts produced via

this AM process are essentially traditional photopolymer parts with micro-scale alumina particles suspended in their structures.

After printing is completed, the parts are separated from the build platform and cleaned with isopropyl alcohol to remove excess resin. Parts are then dried and placed into a high temperature furnace. With an appropriate sintering cycle (section 3.3.2), the polymer compounds present in the green part are volatilized and escape from the part. The ceramic particles then sinter together to form a theoretically pure~~ly~~ ceramic part.

3.2.2 Creation of Slurry

The ceramic slurry is created by the precise mixing of polymer compounds, stabilizers, and alumina particles. This recipe was heuristically developed over the course of this work. The mixing ratios for the ceramic slurry are presented below in Table 1.

Resin Composition	Solid loading (wt%)	Function
Alumina (particle size < 10 µm) (Sigma Aldrich)	70	Ceramic
Autodesk Ember Standard Clear (Colorado PPS)	13	Photopolymer Resin
1,6 Hexanediol Diacrylate	11	Polymer Resin
Variquat 42 dispersant	2	Dispersant
Acetone	3.5	Solvent
Diphenyl (2,4,6-trimethylbenzoyl) phosphine oxide aka TPO	0.5	Photo-initiator Compound

Table 1: Alumina Slurry Composition

These components are individually weighed on a precision balance, and then combined into a glass bodied commercially available countertop blender. The blender helps to fully mix the slurry, ensure proper distribution of particles, and to quickly process large batches. A glass-

bodied blender was chosen because the polymer components can react with and degrade plastic components, contaminating the slurry.

3.2.3 Printing Parameters, Limitations, and Challenges

The Autodesk Ember, a 'bottom up' (see Figure 4, section 1.3.1) projection VP system, was used for printing. The Ember platform is capable of producing parts with exceptional resolution. Ceramic parts with a feature size of 200 μm have been previously produced using this platform [18]. Parts were printed with the process parameters shown in Table 2. These parameters were initially chosen based on measurements of cure depth versus time performed on the ceramic slurry, and then heuristically tuned via a trial and error process to enable successful prints.

Parameter	Value
Layer Height	25 μm
Tray Rotation	60°
First Layer Exposure	2 s
First Layer Separation Velocity	4 rpm
Burn In Layer Exposure	1.5 s
Burn In Layer Separation Velocity	4 rpm
Number of Burn In Layers	4
Model Layer Exposure	1.5 s
Model Layer Separation Velocity	6 rpm

Table 2: Autodesk Ember Key Print Parameters

Bottom up VP systems, such as the Ember platform, are inherently limited by adhesion issues. Parts with a large area of contact between the build platform and projection window increase adhesion and can result in jams and sticking. The inclusion of ceramic particles in the slurry exacerbates this problem, analogous to adding sand to lubricating oil. To properly print, a cured layer must adhere to the build platform, but not to the projection window. This

contradiction in goals inherently limits the maximum viscosity of the printing slurry, which in turn limits the maximum alumina solid loading, and therefore final part density.

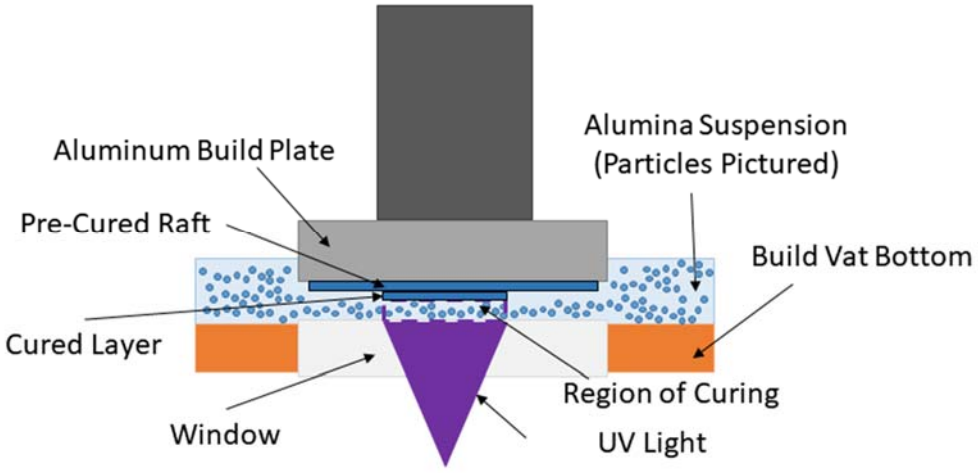

Figure 17: Illustration of Ember Operation

To prevent adhesion issues and maintain a high solid loading, a 'raft' based method of printing was developed (Figure 17). After the slurry is prepared, the printer is initially calibrated with an excess of downward pressure between the build platform and window. This extra force causes strong adhesion of the cured resin to both the build platform and the projection window by ensuring the build platform, slurry, and projection window are in intimate contact. Further study is required to determine the exact cause of this effect. The entirety of the build area is cured during this initial exposure. After a single layer exposure, the build is canceled. The build platform is manually separated from the projection window, with care taken to preserve the film on the surface of the build platform. The build platform, with its raft, are cleaned with isopropyl alcohol and then replaced in the printer. The printer is recalibrated with the standard amount of force between the surface of the raft and the projection window, and the build is commenced. Newly cured layers will adhere to the raft, whereas they would not adhere to the bare aluminum

build platform (Figure 14). It is suspected that the cured polymer is crosslinking to the polymer material in the raft, enabling this adhesion. This process enables the printing of higher viscosity materials on the Ember system.

3.3 Post Processing and Sintering of Alumina Produced via VP

3.3.1 Part Removal and Cleaning

When a print is completed, the build platform is removed from the printer and excess resin is flushed from the part using a hand squeezed bottle of 99% isopropyl alcohol. The part is then carefully separated from the raft using a paint scraper. Great care must be taken to avoid damage to the part or operator. Once parts have been removed and cleaned, they are left to air dry on a paper towel.

3.3.2 Sintering

After the parts have dried, they are placed in an alumina crucible, and then inserted into a high temperature tube furnace with a controlled atmosphere (Figure 18).

Figure 18: Tube Furnace

The furnace is sealed, and a steady flow of compressed air, provided by a building wide compressed air system, is initiated through the furnace. The oxygen present in the compressed air environment allows the photopolymer material to cleanly burn off.

The furnace is programed with a firing schedule (Figure 19) tailored to effectively volatilize the polymer components from the part while limiting shrinkage, cracking, and deformation of the part. This firing schedule was created through a combination of Thermal Gradient Analysis (TGA) and trial and error [18]. Shrinkage has been characterized to be roughly 10% in each linear dimension.

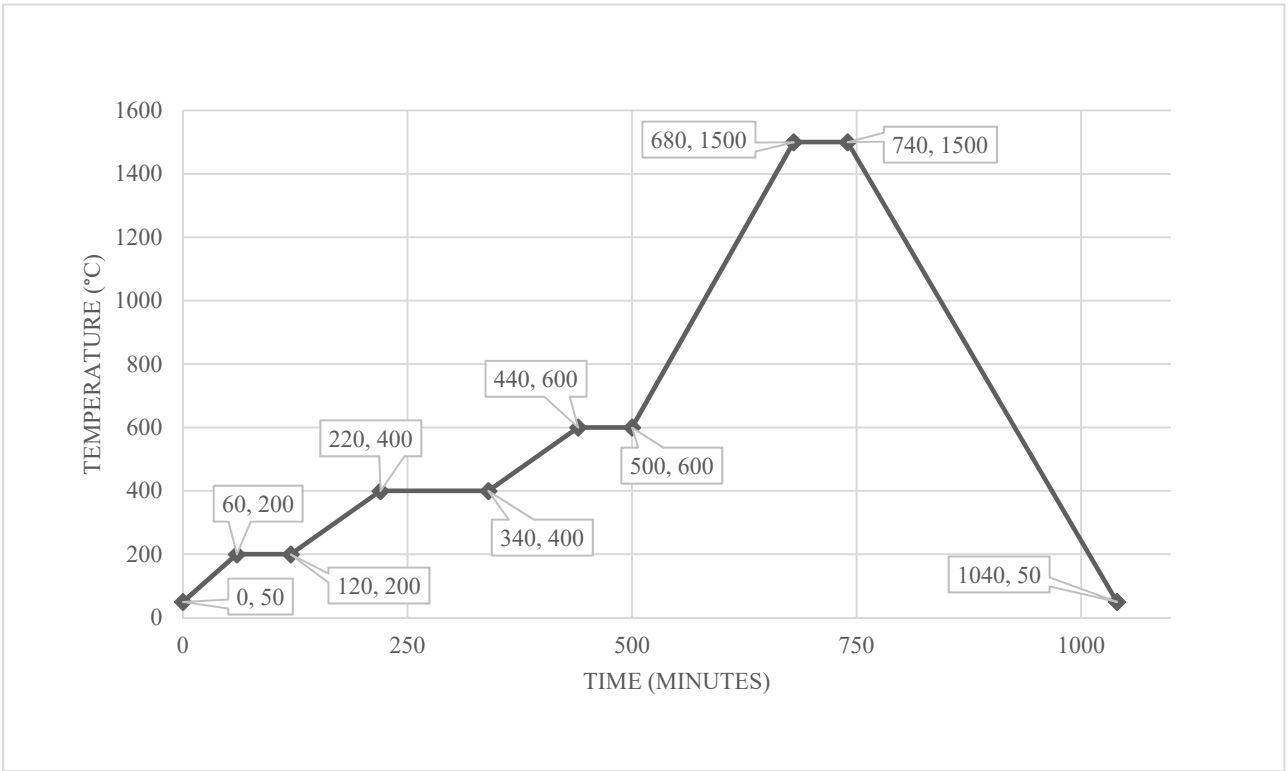

Figure 19: Alumina Firing Schedule

3.3.3 Sintering Induced Shrinkage Compensation

To effectively measure the permittivity and loss tangent of the material, the sample must fit very snugly in the waveguide. In order to ensure a tight fit the samples were slightly enlarged, beyond the enlargement required to compensate for shrinkage during sintering. An additional 1% enlargement factor was applied to the parts during build preparation. The excess material was carefully filed away to ensure the fit inside the sample holder was tight. The accuracy of the measurement technique used is highly dependent on the sample fit in the waveguide.

4 MEASUREMENTS AND DATA PRESENTATION

Ceramic parts, designed to fit the available test fixture, are printed at various relative densities. These parts are printed using the same printing parameters and slurry composition, and are sintered in the same environment with the same firing schedule. After sintering, each part is inserted into a calibrated waveguide test fixture. The scattering parameters (S-Parameters) of the test fixture are measured. The permittivity, permeability, and loss tangent for the material are then numerically de-embedded from the S-parameters and averaged; these points are plotted against relative density and compared with the Weiner bounds.

4.1 PERMITTIVITY MEASUREMENT TECHNIQUE AND RESULTS

The apparatus for making measurements of relative permittivity is a Rhode and Swartz ZVA-50 Vector Network Analyzer (VNA) connected to a short segment of WR-90 waveguide (Figure 20). WR-90 operates in the X-Band (8-12.5 GHz), This operating band was chosen due to its ubiquity in high performance radar systems. The waveguide is used as a sample holder into which sample materials are loaded with identical overall dimensions, but different relative densities. The sample holder is 3.556 mm (0.14 inches) long, less than ¼ of the wavelength of interest to eliminate ¼ λ effects and phase issues, and has an interior dimension of 10.16 mm x 22.86 mm (0.4 inches x 0.9 inches).

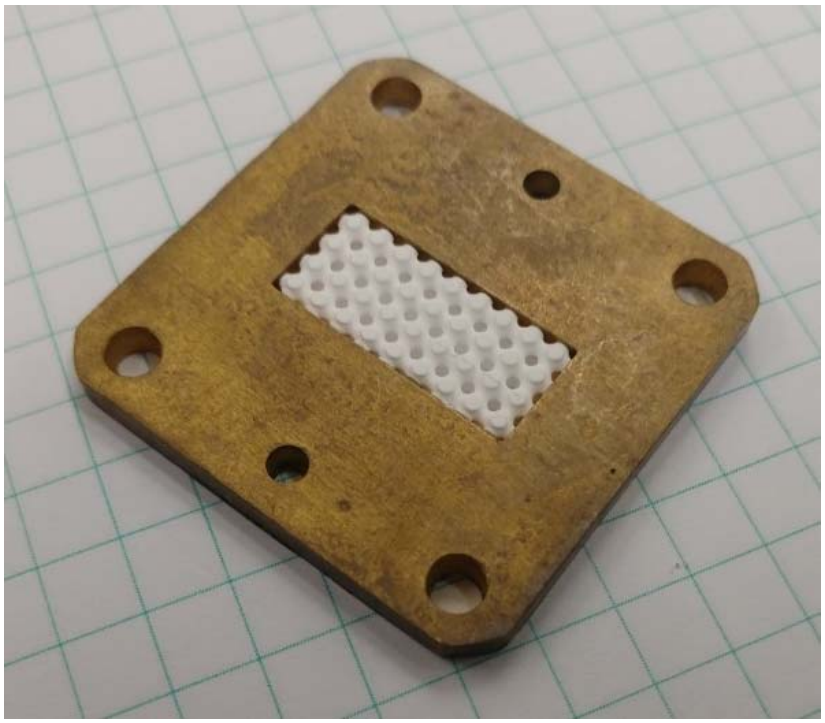

Figure 20: 60% designed density sample pictured resting in WR-90 sample holder

After printing and sintering, each sample is carefully filed to ensure a tight fit in the waveguide (the 50% dense sample was damaged during cleaning and fit loosely in the sample holder). The waveguide segment and a test sample are pictured in Figure 21. S-parameters for each structure are exported from the VNA and used to calculate the permittivity. Coaxial feeds to WR-90 adapters are affixed to the test stand to minimize cable movement and improve the repeatability of the measurement. The VNA is recalibrated using a WR-90 calibration kit between each set of measurements; two separate sets of measurements are made on each series of samples. The permittivity is later extracted from the S-parameters, using the new non-iterative (NNI) method [19].

4.2 DENSITY MEASUREMENT TECHNIQUE

The bulk density of the printed ceramic material was measured using the ASTM B962 – 15 [20] standardized Archimedes measurement. This measurement technique uses oil impregnation under low pressure and liquid displacement to accurately measure the bulk density of sintered solids. Solid cylinders are printed and sintered. Their mass is measured on a precision balance (M_{clean}). These cylinders are then placed in a container of oil and held under low-pressure conditions for an hour. The oil impregnates the parts, filling microstructural voids, and the mass of the parts is measured again (M_{oil}). The parts are then submerged in water and the mass is again measured ($M_{oil+water}$). Using the three measured values of mass and the known density of water at room temperature (ρ_{water}), the bulk density of the parts is calculated using Equation (6).

$$\rho = \frac{M_{clean}\,\rho_{water|23.3℃}}{M_{oil} - M_{water+oil}} \tag{6}$$

4.3 DATA PRESENTATION

The bulk density of the alumina material printed using the process outlined in this paper was measured to be 2.04000± 0.00432 g/cm^3 using the measurement process described in section 4.2.

The relative permittivity (ε_r) and permeability (μ_r) of each structure is measured across frequency in the X-Band (8-12.5 GHz) using the new non-iterative (NNI) method published by Rhode and Swartz [19]. This calculation results in several valid data points across the range of frequencies tested. Data points are considered valid in this method when the measured permeability (μ_r) is equal to roughly 1, other measured data is non-physical as the material is nonmagnetic. This process was prescribed by the manufacturer. An example output of this method is shown in Figure 22, with the valid data points labeled.

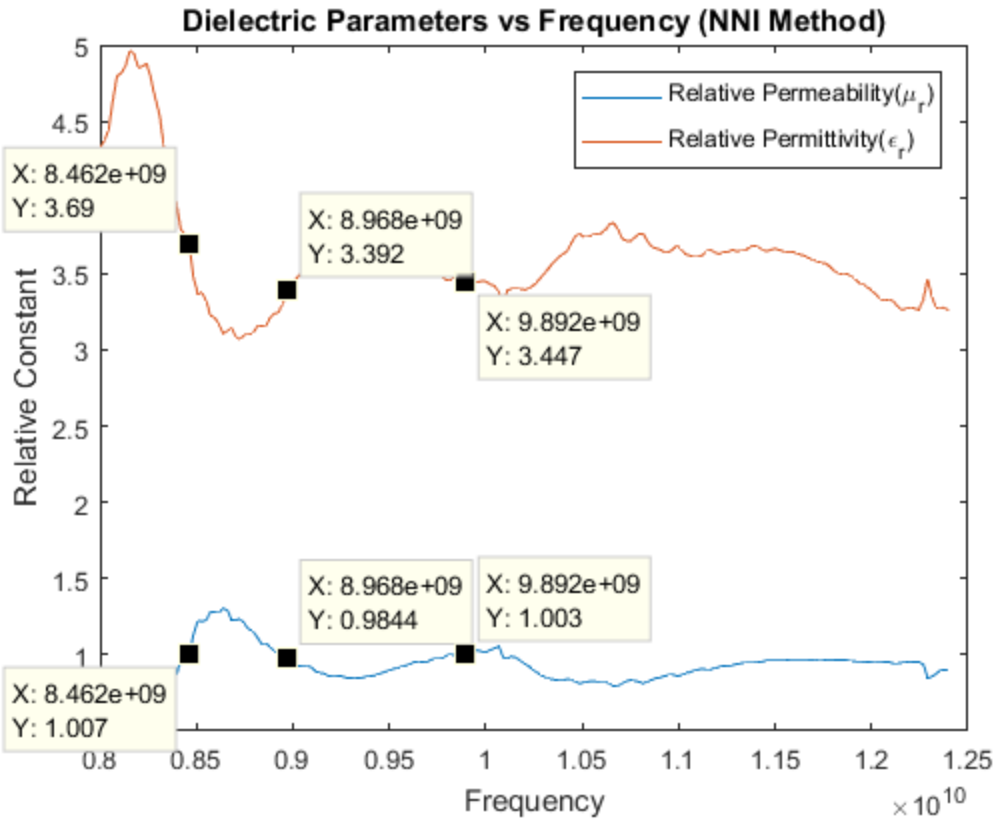

Figure 21: Extracted Dielectric Parameters for 100% Dense Sample

Table 3 shows the arithmetic average value of permittivity and the standard deviation of each measurement set along with the value of permittivity for each sample density predicted by the upper Wiener bound shown in equation (4). The measured loss tangent for each structure is also presented in Table 3. Further discussion of the anomalous 50% dense sample is located in the discussion section.

Relative Density	Predicted Permittivity	Measured Permittivity	Measured tan(δ)
100%	3.60	3.60 ± 0.151	6.46 x10^{-3}
70%	2.82	2.92 ± 0.158	4.45 x10^{-3}
60%	2.56	2.60 ± 0.147	5.53 x10^{-3}
50%	2.30	2.09 ± 0.121	3.73 x10^{-3}
40%	2.04	2.06 ± 0.101	6.63 x10^{-3}
30%	1.78	1.74 ± 0.070	4.22 x10^{-3}

Table 3: Measured Relative Permittivity and loss Tangent of Samples

The predicted and measured values of the effective permittivity from Table 3 are also plotted below in Figure 23. The plotted points are the average measured values of the relative permittivity of the sample. The error bars represent the standard deviation of each measurement. The predicted values given by the upper and lower Wiener bounds are also plotted as a line for all densities.

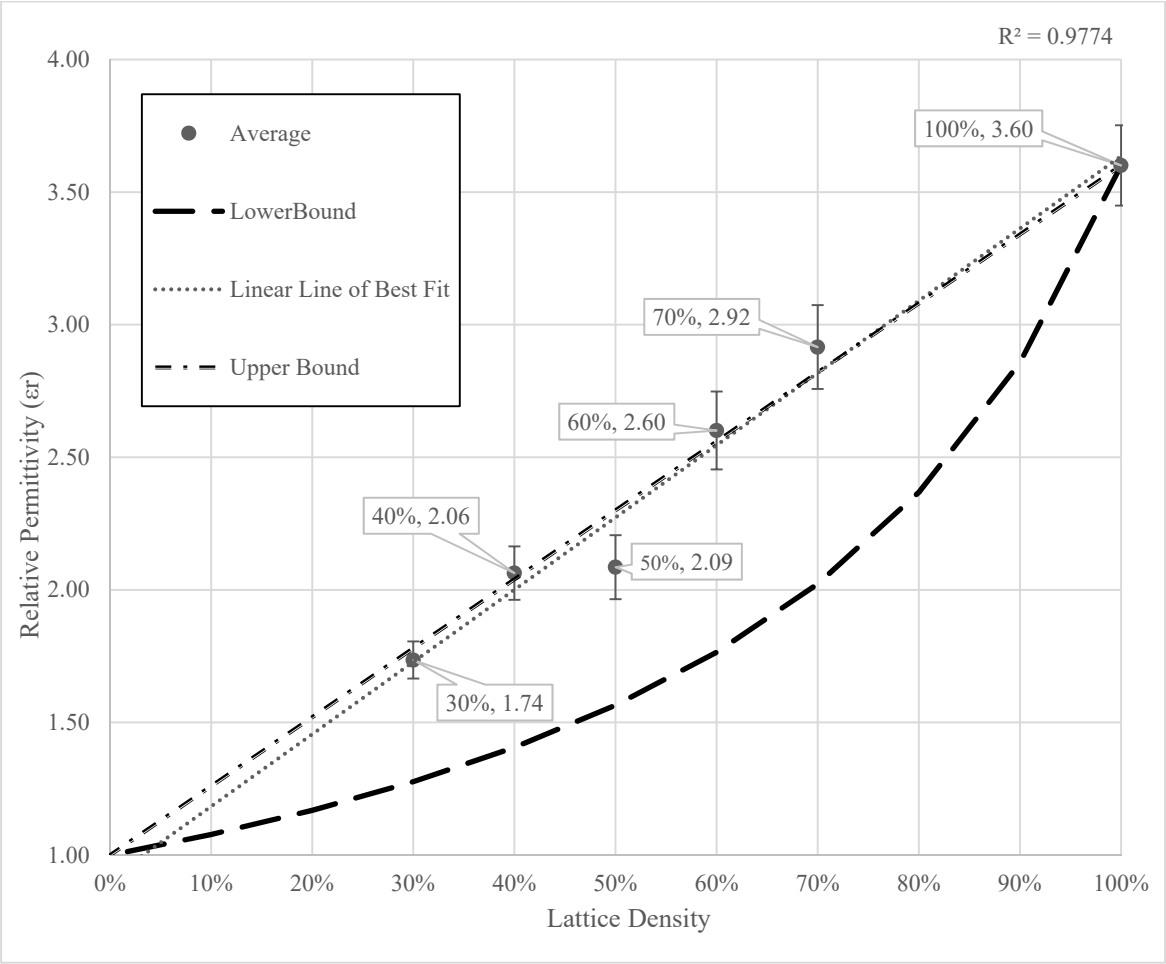

Figure 22: Average Measured Relative Permittivity and Upper Wiener Bound Plotted Against Designed Density

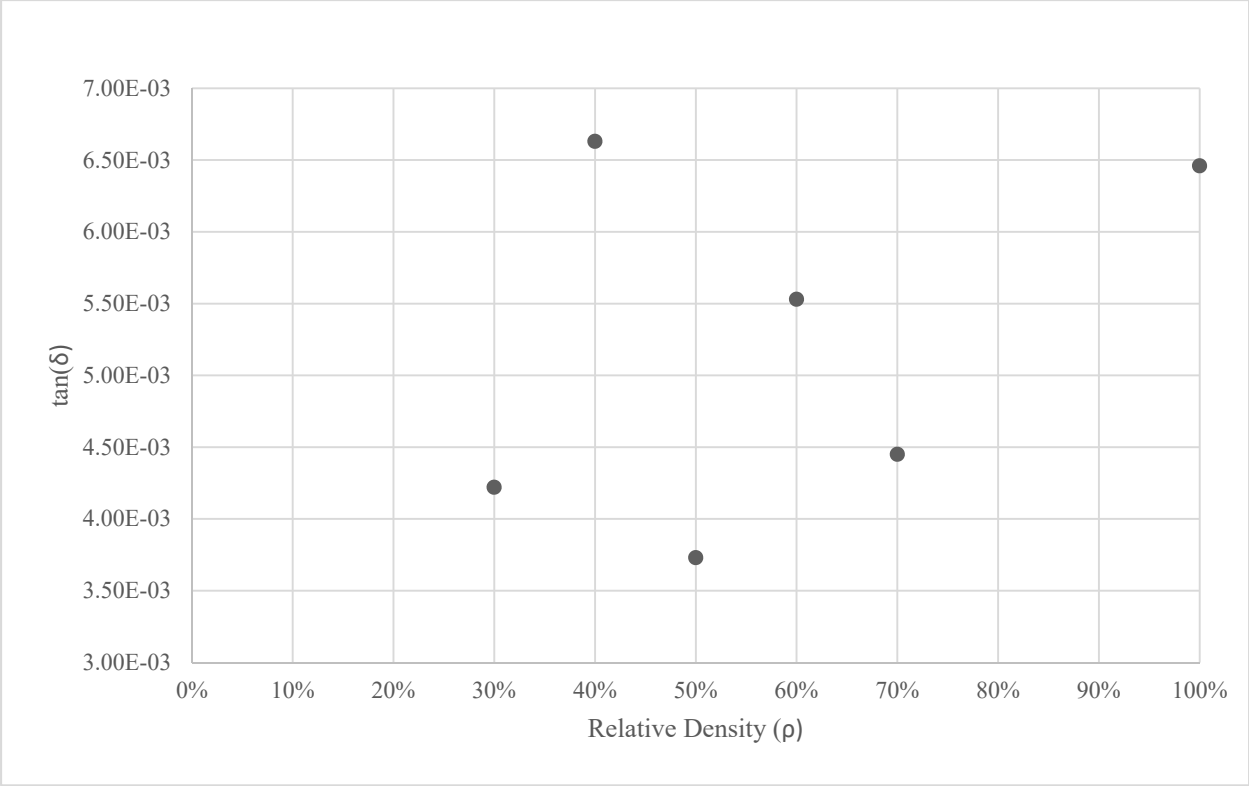

Figure 23: Measured Loss Tangents Plotted against Relative Density

The measured loss tangents are plotted against the relative densities in Figure 24. Loss tangent measurements were considered valid when magnetic losses were equal to zero (nonmagnetic material), and the dielectric loss was positive (negative loss is unphysical). There was only a single valid data point for each sample. It can be seen that there is no clear relationship between the loss tangent and the macro-scale relative density. Alternative measurement methods of the loss tangent, such as measurement of the Q of dielectric resonators, would likely produce many more valid data points across the measured frequencies.

5 DISCUSSION

The average trend of the relative permittivity measurements shown in Table 1 is linear across the range of test frequencies, as shown graphically in Figure 22. It is observed that the measured values of the dielectric constant closely match the upper Wiener bound. The 50% dense sample does not fall on the linear fit line. Upon close inspection of the sample it appears that a corner of the part is damaged, causing it to fit loosely in the waveguide. This damage, as well as the relative difficulty of ensuring that the sample remains stationary within the waveguide while the measurements are performed, likely led to the deviation of this sample point from the linear trend.

The dielectric constant of the 100% infill part was measured to be 3.6, which is relatively low compared to the expected dielectric constant of alumina (9.8) [12]. However, the bulk density was also observed to be much lower (2.04 g/cm^3), which is only 51.6% of the expected value (3.97 g/cm^3) [12]. The predicted value of permittivity of an alumina structure with roughly 50% porosity matches the measured data closely [13]. This low density of the printed material is a result of the limitations of the printing platform. The Autodesk Ember is what is known as a 'bottom up' system, where the resin is cured between a window and moving build platform by a UV source illuminating from the bottom. Higher viscosity suspensions generate excess adhesion between the build platform and window, causing jamming during printing. This problem is not present in so called 'top down' systems, where the resin is cured by the UV source from above. Top down systems have been previously shown to produce alumina dielectrics with higher permitivitties ($\varepsilon_r = 9.1$) [17]. This is due to the ability of the top down system to print a resin with a much higher solid loading percentage than the bottom up system in use by the author. A top

down system is not limited by the adhesion issues that occur in bottom up systems, as there is no window.

The loss tangent measurements show a material roughly an order of magnitude less lossy than the polymers and polymer composites used in previous work [7] [21]. The measured value is more lossy than the accepted value of the loss tangent of alumina (10^{-4}) [12] by roughly an order of magnitude. This loss may be attributed to the high micro porosity (low density) of the alumina produced through this printing process [13]. Additional potential sources of loss include leftover combustion byproducts from the sintering process. It has previously been shown that alumina printed with VP processes can achieve a very low loss tangent ($1.3 \text{ X } 10^{-4}$) [17]. Increased solid loading of the alumina powder, as well as improved resins, should enable the production of structures with properties that approach the previously published values.

While the author has full confidence in the measured permittivity values using the NNI method, the measurements of the loss tangent are less certain. Further measurements of the loss tangent using alternative methods, such as the construction and measurement of a high Q dielectric resonator using these materials, may~~will~~ provide a more certain measurement of the loss tangent.

The Autodesk Ember has been shown to produce alumina ceramic structures with a feature size of 200 µm [18]. Based on this specification, it is possible to create compound dielectric structures with a feature size that satisfies the $1/10^{th}$ wavelength requirement for devices operating at frequencies up to 110 GHz. This will enable application of this process in high frequency microwave and millimeter wave circuits and devices.

6 MULTI-MODAL PRINTING AND EMBEDDING

Additional work was conducted studying the use of a unique multi-process printer to create alumina and alumina composite structures. This work serves primarily as a proof of concept, and is presented in following subsections.

6.1 MULTI-MODAL PRINTER

A multi-modal printer system uses more than one distinct printing process to create a single part. The multi-modal printer in the DREAMS Lab (Figure 25) is capable of combining material jetting, binder jetting, vat photopolymerization, and material extrusion technologies into a single system. This unique combination of printing processes enables the creation of novel multi-material parts. [22]

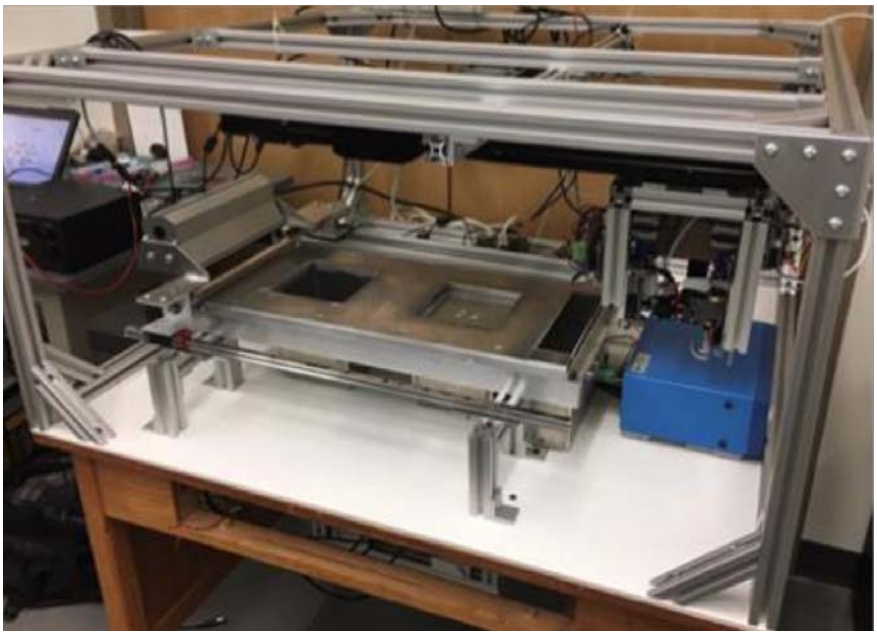

Figure 24: Multi-Modal Printer Located in DREAMS Lab

6.2 ADVANTAGES OF MULTI MODAL SYSTEMS

As the multi-modal system in use by the author is capable of simultaneously performing vat photopolymerization and paste extrusion, multiple distinct materials, each with unique processing requirements, can be deposited in a single print. This ability enables the creation of unique composite structures. Materials with compatible firing schedules can be printed, and sintered, together.

Two additional materials in particular are interesting for potential applications for high performance EM structures. Nickel is a high temperature (1455 °C melting point) metal with a reasonably high electrical conductivity (14.3 ℧/m) [23]. Ferrite (an iron oxide ceramic) is a non-conductive material with a high relative permeability (dependent on exact composition). The freeform fabrication of a structure consisting of arbitrary arrangements of these three materials (alumina, ferrite, and nickel) could enable the production of highly tailored electromagnetic structures, with fully definable permittivity and permeability throughout the structure, as well as arbitrarily placed conductive elements.

6.3 ALUMINA – FERRITE STRUCTURES

6.3.1 Process Adjustments

The multi-modal printer used to produce the composite parts uses a top-down VP system, as opposed to the Ember's bottom up configuration. While in future work this may enable the use of higher viscosity slurries, these parts were printed from the same alumina mixture presented in Section 3.2.

The top-down VP system does present various complications, however. Due to the lack of pressure between the window and build platform present in the bottom up system, adhering

the first layer to the build platform is a challenge. A modified variant of the raft technique used in the bottom-up system has been developed to alleviate these issues. To print the raft, the build platform is raised to its standard position, and then a glass slide is pressed down on the build platform. The first layer is cured through this glass slide. The pressure provided by the glass slide causes the cured polymer to better adhere to the build platform. The slide is then carefully removed and the print is conducted using the standard top-down printing method.

A prepared ferrite paste generously provided by Dr. Guo-Quan Lu at Virginia Tech was extruded from the printer's paste-dispensing nozzle. This paste was extruded into printed channels in the part. This required raising the build platform above the surface of the vat, cleaning uncured resin from the printed channel. After the paste is extruded, the build platform is lowered back to its printing position and the print is resumed. This process, as well as the generation of the raft using the glass slide, is shown in Figure 25. Pictures of the extruded ferrite and the finished fired with an attached rare earth magnet are shown in Figure 26, left and right, respectively.

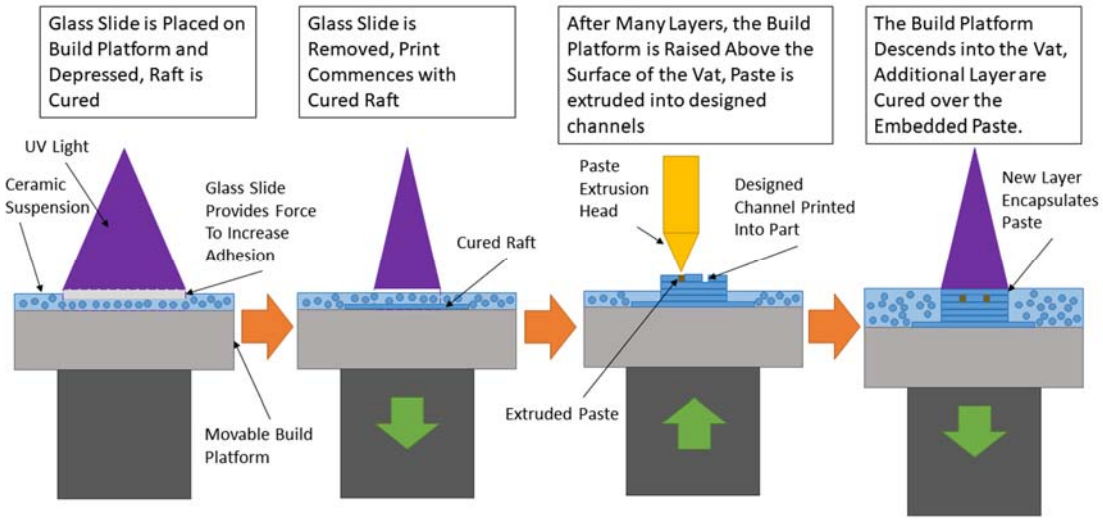

Figure 25: Multi-Modal Printing and Embedding Process

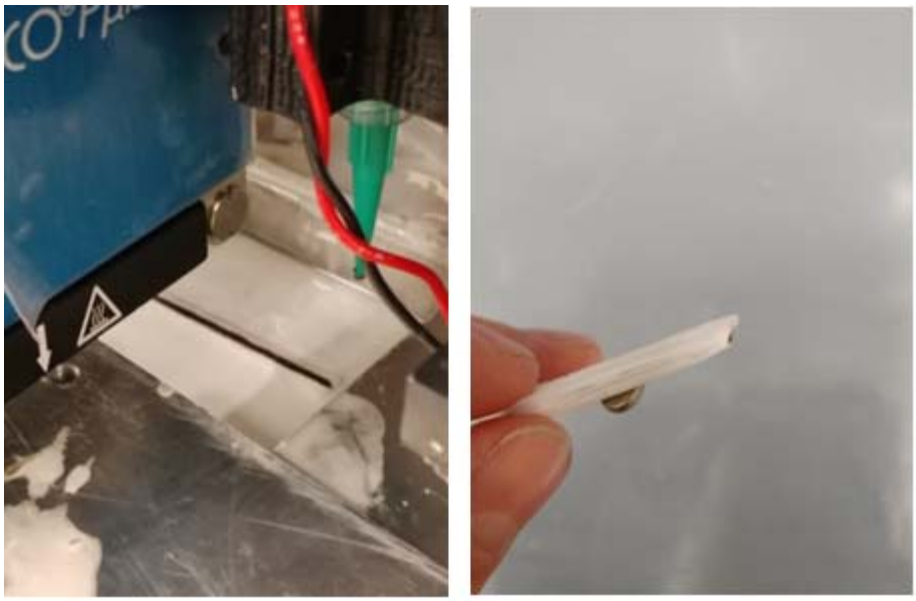

Figure 26: Ferrite Paste Extruded into Alumina VP structure (Left), Post Sintering Structure with Magnet Attracted to Ferrite Core (Right)

6.3.2 Embedding of Nickel Wires

Although a nickel based paste extrusion technique was conceived, proof of concept tests were carried out with already available pure nickel wire. This wire is embedded in much the same way as the ferrite paste. Nickel wire is manually placed into designed printed channels during a pause in the print, and the print is then resumed. This process has previously been used with various components in various other printing processes, including high frequency transmission line structures [14].

6.3.3 Firing Limitations

In order to enable the production of structures consisting of nickel, ferrite, and alumina, the firing schedule must be adjusted. A maximum firing temperature of 1350 °C was selected to avoid melting nickel components while still sintering ceramic portions by providing a factor of safety of about 100 °C between the sintering temperature and the melting point of nickel (1455 °C) [23]. Additionally, the firing schedule was amended to include temperature holds critical to the

proper sintering of the provided ferrite paste, provided by Dr. Lu's research group. This modified firing schedule is presented in Figure 27.

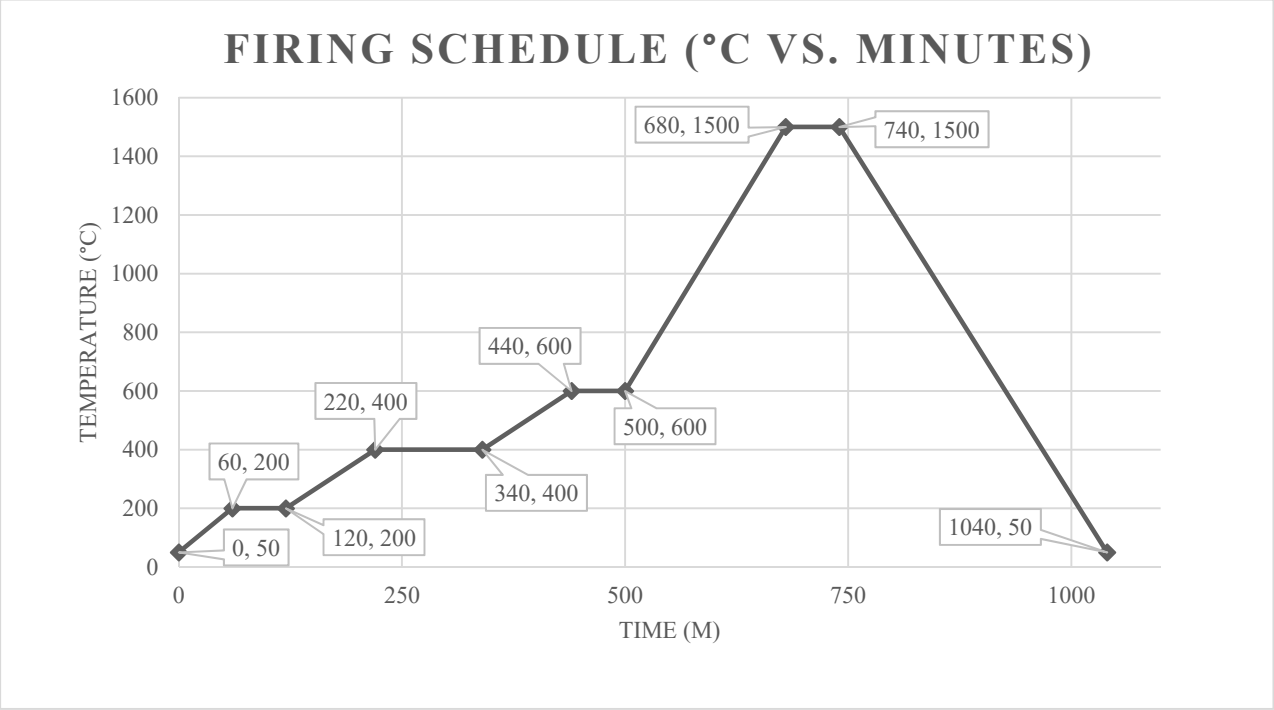

Figure 27: Modified Firing Schedule

6.4 Discussion of Multi-Modal Printing

Multi-modal prints including extruded ferrite paste and manually embedded nickel wires were produced and sintered. The nickel wires survived the sintering process, although cracking occurred in the ceramic due to differential shrinkage (Figure 28). Determining the proper design tolerances for embedding nickel wires may prevent this cracking in the future. The nickel wire underwent heavy surface oxidation during the sintering process (Figure 28); however, the oxidation could be easily scraped away from the wire and the wire remained ductile. Alternative sintering parameters could potentially reduce, reverse, or altogether eliminate this oxidation. While an oxygen environment is required to properly volatilize the polymer compounds in the

ceramic structure, a pure nitrogen or hydrogen environment could be created mid-sintering through the use of a gas mixer. A nitrogen environment would inhibit oxidation of the metal, while a hydrogen environment not only inhibits, but also reverses the oxidation process due to hydrogen's high reactivity with oxygen.

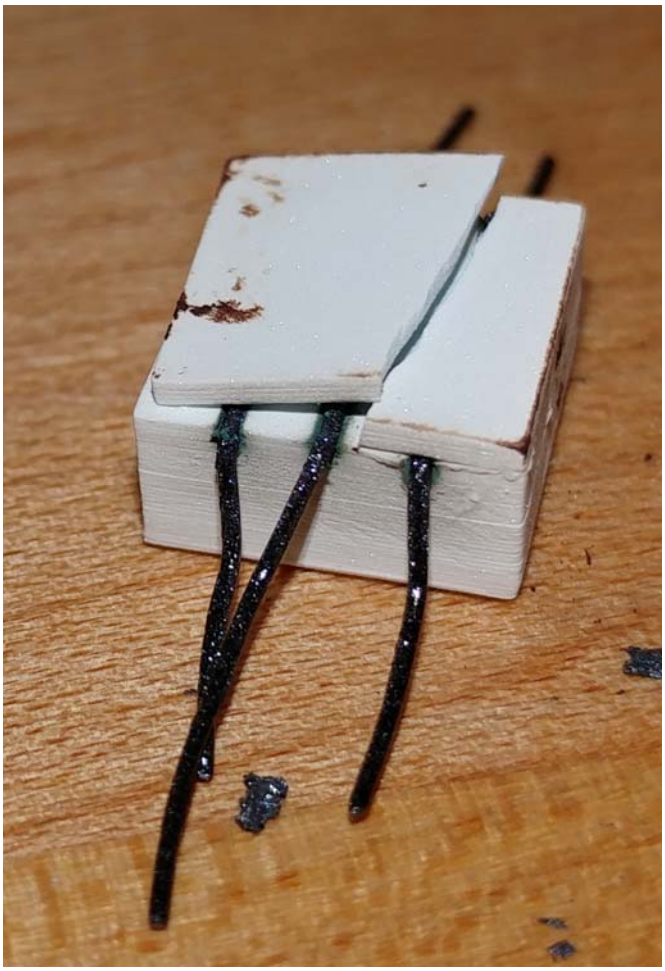

Figure 28: Sintered Nickel Alumina Structure

The ferrite nickel composite parts printed and sintered without issue. No cracking or deformation was observed. The author is unaware of any similar structures in published literature. The ferrite attaches strongly to permanent magnets and appears to be strongly bonded to the ceramic structures. In the future, the ferrite may be permanently magnetized through the application of a magnetic field to the furnace during the sintering cycle. Further work is needed

to understand the full impact such structures could have on the state of the art, and the interaction of the two separate materials at their interface.

7 CONCLUSIONS

7.1 SUMMARY

Additively manufactured alumina structures have been created at varying relative densities, and the effects of the differing geometries on their relative permittivity have been characterized in the X-Band. It can be concluded that alumina structures with a specified permittivity can be produced via a VP and post processing production process. These structures follow the theoretical upper Wiener bound when the feature size of the structure remains less than 1/10 of a wavelength.

As alumina is a ceramic, these structures are capable of withstanding very high temperatures, so they may be useful in applications relevant to high temperature environments. The permittivity of these structures can be easily changed by varying the lattice density, allowing for a large range of relative permitivitties to be produced in different shapes and sizes within a single dielectric structure.

Nickel –Alumina and Ferrite – Alumina composite structures can be created using a multi-modal printing system and can be successfully co-fired. As magnetic permeability is the dual of electric permittivity, there is reason to believe that the effective permeability can easily be varied in the same manner by varying the concentration of ferrite within a lattice. Structures with fully definable permittivity, permeability, and conductive elements could be created using these processes.

7.2 CONTRIBUTIONS

1. The effects of relative density on the permittivity of dielectric structures have been characterized to a degree that it would be possible to create structures of a desired permittivity through geometric design.

2. A novel method for printing ceramic-photopolymer suspensions using a raft has been developed. This technique is equally applicable to both bottom-up and top-down systems. The use of increased pressure to increase photopolymer adhesion to the build platform helps to enable the printing of higher viscosity materials, enabling the production of higher density parts.

3. Novel ferrite-alumina and nickel-alumina structures have been printed. With continued work, such structurers can create many different electromagnetic structures, theoretically including non-reciprocal devices, such as circulators, at a very small scale.

8 FUTURE WORK

The results presented here provide some indication of directions for future improvements. One such goal is to reduce the loss of the alumina material. New resin formulations may help to reduce the loss of the material. A higher solid loading of ceramic particles in the ceramic slurry could be used to create higher density parts with potentially higher effective dielectric constants. Binder jetting may be explored as an alternative to vat photopolymerization for creating ceramic structures to potentially accomplish these goals. It has been shown that binder jetting is capable of producing very dense copper parts [24, 25], and the methods explored in these sources may also work for alumina structures. Binder jetting has an additional, less obvious, advantage over VP in that it does not produce large amounts of hazardous waste as a result of normal operation of the printing process.

Use of extruded nickel paste in addition to ferrite pastes for the inclusion of multiple materials into the ceramic components could also be explored. The potential applications of varied lattice density of extruded nickel and ferrite is a promising direction for future work, since controlling both the permittivity and permeability of electronic structures has the potential to enable the development of novel electromagnetic materials that could be useful in a number of fields.

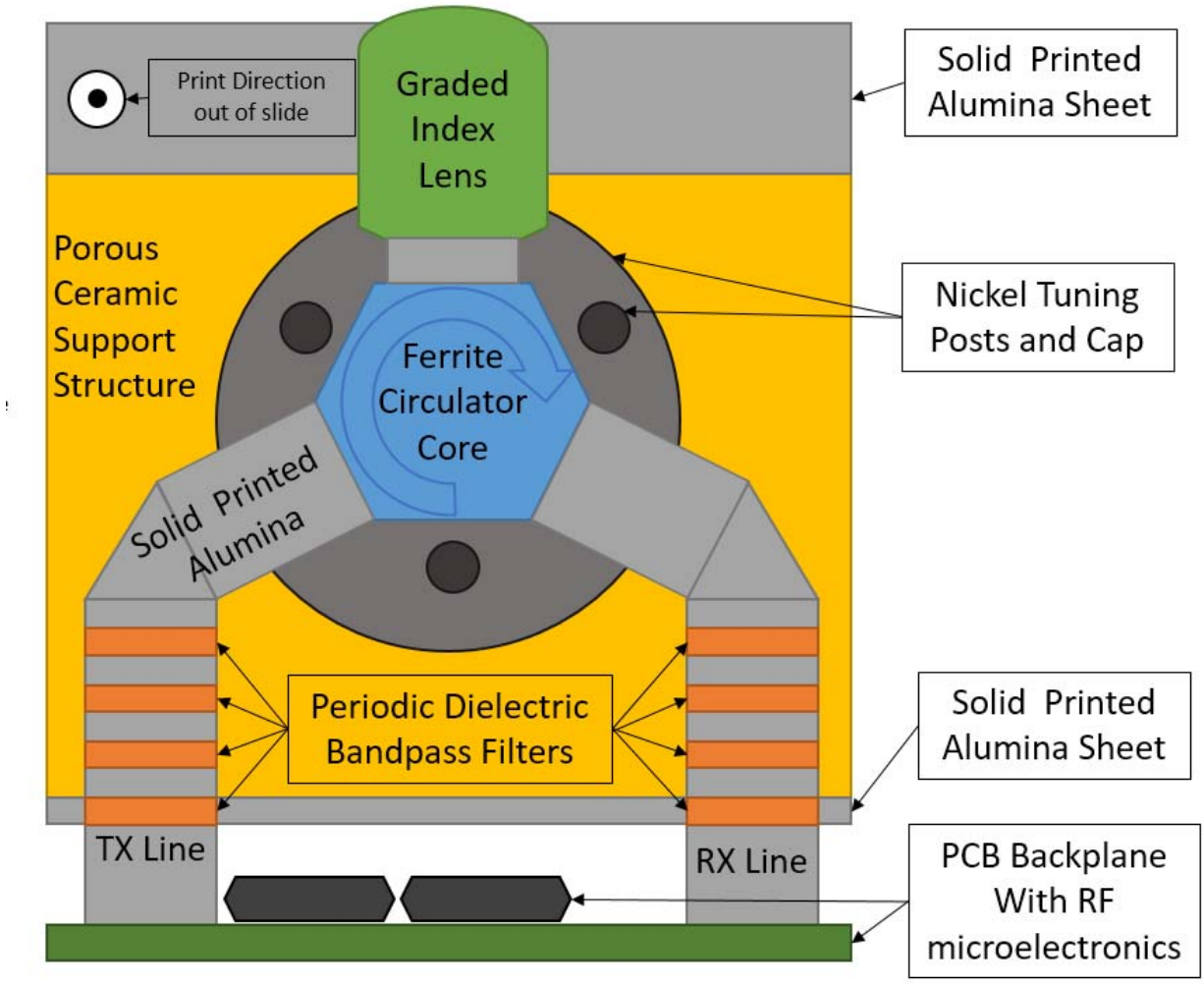

Figure 29: Potential Future Application of Multi-Modal Printing for Electromagnetic Structures

Figure 29 shows a notional design of an embedded circulator with dielectric waveguide feeds. Further work could include the creation of integrated antenna modules including a metamaterial antenna, an embedded circulator, and integrated dielectric waveguides and filters. Such a structure would be able to potentially withstand temperatures in excess of 1500 °C.

An example of a practical system based on outcomes of this initial study could include any application in which electromagnetic structures capable of withstanding harsh and extreme environments offer benefits. One such example is combining drilling and remote sensing for oil and gas exploration. Ground penetrating radar located within a steerable drill could help locate optimal exploration regions and improve the accuracy of drilling for a variety of applications, but the high temperature environment would require electromagnetic structure capable of withstanding very high temperatures. An additional example might be communication systems on spacecraft and/or missile systems re-entering Earth's atmosphere or flying supersonically at low altitudes. Antenna embedded in ceramic substrates with tunable dielectric properties could be useful in such applications. It is hoped that the research reported here may stimulate future applied research in these and other areas.

9 REFERENCES

[1] K. Prakasha, T.Nancharaihb and V. Raoc, "Additive Manufacturing Techniques in Manufacturing - An Overview," *Materials Today: Proceedings,* vol. 5, pp. 3873-3882, 2018.

[2] Y. Guo, H. S. Patanwala, B. Bognet and A. W. Ma, "Inkjet and inkjet-based 3D printing: connecting fluid properties and printing performance," *Rapid Prototyping Journal,* vol. 23, no. 3, pp. 562-576, 2017.

[3] N. Travitzky, A. Bonet, B. Dermeik, T. Fey, I. Filbert-Demut, L. Schlier, T. Schlordt and P. Greil, "Additive Manufacturing of Ceramic-Based Materials," *Advanced Engineering Materials,* vol. 16, no. 6, pp. 729-754, 2014.

[4] S. J. Orfanidis, Electromagnetic Waves and Antennas, New Brunswick: Rutgers University, 2016.

[5] N. G. Research, Artist, *Split-ring_resonator_array_10K_sq_nm.jpg.* [Art]. NASA, 2006.

[6] I. Aghanejad, H. Abiri and A. Yahaghi, "Design of High-Gain Lens Antenna by Gradient-Index Metamaterials Using Transformation Optics," *IEEE TRANSACTIONS ON ANTENNAS AND PROPAGATION,* vol. 60, no. 9, pp. 4074-4082, 2012.

[7] F. Castles, D. Isakov, A. Lui, Q. Lei, C. Dancer, Y. Wang, J. Jamurudin, S. Speller, C. Grovenor and P. Grant, "Microwave dielectric characterisation of 3D-printed BaTiO3/ABS polymer composites," *Scientific Reports,* vol. 6, no. doi: 10.1038/srep22714 (2016)., 2016.

[8] S. Torquato, Random Heterogeneous Materials Microstructure and Macroscopic Properties, New York: Springer, 2002.

[9] Univeristy of Cambridge, "Derivation of the rule of mixtures and inverse rule of mixtures," Univeristy of Cambridge, 2018. [Online]. Available: https://www.doitpoms.ac.uk/tlplib/bones/derivation_mixture_rules.php. [Accessed 4 May 2018].

[10] P. Patnaik, Handbook of Inorganic Chemicals, New York: McGraw-Hill, 2003.

[11] P. Auerkari, Mechanical and physical properties of engineering alumina ceramics, ESPOO: TECHNICAL RESEARCH CENTRE OF FINLAND, 1996.

[12] Microwaves101, "Alumina 99.5%," Microwaves101, 2017. [Online]. Available: https://www.microwaves101.com/encyclopedias/alumina-99-5. [Accessed 2017].

[13] S. J. Penn, N. M. Alforn, A. Templeton, X. Wang, M. Xu, M. Reece and K. Schrapel, "Effect of Porosity and Grain Size on the Microwave Dielectric Properties of Sintered Alumina," *Journal of the American Ceramic Society,* vol. 80, no. 7, pp. 1885-1888, 1997.

[14] R. L. Dumene, P. Kennedy, C. B. Williams, D. Sweeney and G. Earle, "CREATING EMBEDDED RADIOFREQUENCY STRUCTURES USING POLYJET MATERIAL JETTING," in *International Solid Freeform Fabrication Symposium*, Austin, TX, 2015.

[15] H. Xin and M. Liang, "3-D-Printed Microwave and THz Devices Using Polymer Jetting Techniques," *Proceedings of the IEEE,* vol. 105, no. 4, p. 755, 2017.

[16] M. Lis, M. Plaut, A. Zai, D. Cipolle, J. Russo and T. Fedynyshyn, "High Performance, 3D-Printable Dielectric Nanocomposites for Millimeter Wave Devices," *Applied Materils & Interfaces,* pp. A-H, 2016.

[17] T. Chartier and C. Duterte, "Fabrication of Millimeter Wave Components Via Ceramic Stereo- and Microstereolithography Processes," *The American Ceramic Society,* vol. 91, no. 8, pp. 2469-2474, 2008.

[18] D. C. J. Aduba, K. D. Feller and C. B. Williams, "An Investigation of Build Orientation on Shrinkage in Sintered Bioceramic Parts Fabricated By Vat Photopolymerization," in *Solid Freeform Fabrication 2017: Proceedings of the 28th Annual International Solid Freeform Fabrication Symposium - An Additive Manufacturing Conference*, Austin, TX, 2017.

[19] K. C. Yaw, *<RAC0607-0019_1_4E>,* Munich: Rhode & Schwarz, 2012.

[20] ASTM International, *Standard Test Methods for Density of Compacted or Sintered Powder Metallurgy (PM) Products Using Archimedes' Principle,* Conshohocken, , PA: ASTM.

[21] D. Isakov, Q. Lei, F. Castles, C. Stevens, C. Grovenor and P. Grant, "3D printed anisotropic dielectric composite with meta-material features," *Materials and Design,* vol. 93, pp. 423-430, 2016.

[22] L. B. B. D. A. R. S. B. Z. M. S. W. D. L. W. Y. B. V. Grady W. Wagner, "Design and Development of a Multi-Tool Additive Manufacturing System," in *Solid Freeform Fabrication*, Austin, 2017.

[23] Royal Society of Chemistry, "Periodic Table: Nickel," Royal Society of Chemistry, 2017. [Online]. Available: http://www.rsc.org/periodic-table/element/28/nickel. [Accessed 2018].

[24] A. Y. Kumar, "Effects of Hot Isostatic Pressing on Copper Parts Additively Manufactured via Binder Jetting," Virginia Tech, Blacksburg, 2018.

[25] A. Kumar, Y. Ba, A. Eklund and C. B. Williams, "Effects of Hot Isostatic Pressing on Copper Parts Fabricated via Binder Jetting," in *45th SME North American Manufacturing Research Conference*, LA, 2017.

[26] S. Zhang, Y. Vardaxoglou, W. Whittow and R. Mittra, "3D-Printed Graded Index Lens for RF Applications," in *Proceedings of ISAP2016*, Okinawa, Japan, 2016.

[27] W. L. Stutzman and G. A. Thiele, Antenna Theory and Design (3rd Edition), New York: Wiley, 2013.

[28] B. Perez and C. Williams, "Characeterization of In-situ Conductive Paste Extrusion on PolyJet Substrates," in *International Solid Freeform Fabrication Symposium*, Austin, TX, 2014b.

[29] N. Meisel, A. M. Elliot and C. B. Williams, "A procedure for creating actuated joints via embedding shape memory alloys in PolyJet 3D Printing," *Journal of Intelligent Material Systems and Structures,* no. doi:// 1045389X14544144, 2014.

[30] A. M. Elliott, O. S. Ivanova and C. B. Williams, "Inkjet Printing of Quantum Dots in Photopolymer for Use in Additive Manufacturing of Nancomposites," *Advanced Engineering Materials,* vol. 15, no. 10, pp. 903-907, 2013.

[31] S. Bukhari, W. Whittow, S. Zhang and J. Vardaxoglou, "Composite materials for microwave devices," *ELECTRONICS LETTERS,* vol. 52, no. 10, pp. 832-833, 2016.

[32] Added Scientific, "Software and Modelling," Added Scientific, [Online]. Available: http://addedscientific.com/resources/software-and-modelling. [Accessed 2017].

[33] H. Zong, X. Liu, X. Ma and S. Lin, "Printed H-plane horn antenna with loaded dielectric-metal composite lens," *IET Microwaves, Antennas & Propagation,* vol. 11, no. 5, pp. 642-648, 2016.